Spectroscopy of SU(4) composite Higgs theory with two distinct fermion representations

Venkitesh Ayyar,[1] Thomas DeGrand,[1] Maarten Golterman,[2] Daniel C. Hackett,[1] William I. Jay,[1]
Ethan T. Neil,[1,3,*] Yigal Shamir,[4] and Benjamin Svetitsky[4]

[1]*Department of Physics, University of Colorado, Boulder, Colorado 80309, USA*
[2]*Department of Physics and Astronomy, San Francisco State University,
San Francisco, California 94132, USA*
[3]*RIKEN-BNL Research Center, Brookhaven National Laboratory, Upton, New York 11973, USA*
[4]*Raymond and Beverly Sackler School of Physics and Astronomy, Tel Aviv University,
69978 Tel Aviv, Israel*

We have simulated the SU(4) lattice gauge theory coupled to dynamical fermions in the fundamental and two-index antisymmetric (sextet) representations simultaneously. Such theories arise naturally in the context of composite Higgs models that include a partially composite top quark. We describe the low-lying meson spectrum of the theory and fit the pseudoscalar masses and decay constants to chiral perturbation theory. We infer as well the mass and decay constant of the Goldstone boson corresponding to the nonanomalous U(1) symmetry of the model. Our results are broadly consistent with large-N_c scaling and vector-meson dominance.

I. INTRODUCTION

Gauge theories coupled simultaneously to more than one fermion representation—"multirep" theories—open a new dimension in the study of gauge dynamics. Apart from the influence of each fermion species on the gauge field and vice versa, phase transitions and symmetry breaking in each species can affect the others dramatically. Of course, QCD already contains light quarks, strange quarks, and heavy quarks, and the influence of each species on the others is an old and continuing object of QCD calculations. The difference is that QCD's quarks are all equivalent, in that a tuning of the masses can change one into another. Fermions in inequivalent representations, on the other hand, enter the dynamics with different strengths irrespective of their masses.

As usual, symmetries offer the clearest perspective on the physics of inequivalent fermions. Each species has its maximal flavor symmetry, while no symmetries mix the different species. If all the fermions are made massless, the chiral symmetries of the species remain distinct. One symmetry could break spontaneously while others do not.

This is a generalization of the old issue of scale separation, which was originally seen as a possible separation of a chiral scale from the confinement scale of the gauge theory [1–3]. It is possible that inequivalent representations, simultaneously coupled to the gauge field, define independent chiral scales. This might find expression in the finite-temperature physics of the theory, in the form of distinct phase transitions for each fermion species as well as for the confinement physics of the gauge field. Alternatively, one phase transition, possibly governed by the largest quadratic Casimir of the fermion representations, might trigger all the others to occur at the same scale.

We present here the first results of our work on the SU(4) gauge theory with $N_f = 2$ Dirac fermions in each of two distinct representations, the fundamental **4** and two-index antisymmetric **6** (a real representation). We have chosen this model because it is close to a model proposed by Ferretti for a hypercolor theory that yields a composite Higgs boson [4,5] and a partially composite top quark [6]. Ferretti's model [7] contains 5 Majorana fermions in the sextet representation and 3 Diracs fermions in the fundamental; simulating this fermion content requires the costly Rational hybrid Monte Carlo (RHMC) algorithm, and so, instead, we study the theory with 4 Majoranas (equivalent to 2 Dirac fermions) in the sextet and 2 Diracs in the fundamental. In Ferretti's model, the massless sextet Majorana fermions Ψ condense to break their chiral symmetry according to SU(5) → SO(5), whereupon the Standard Model's Higgs multiplet appears

---

*ethan.neil@colorado.edu

as Nambu-Goldstone (NG) bosons; our symmetry breaking scheme is[1] $SU(4) \to SO(4)$. The fundamental fermions $\psi^{(4)}$ in Ferretti's model are brought in so that the theory will possess fermionic baryons constructed as $\psi^{(4)}\psi^{(4)}\Psi$ "chimera" bound states, to be used as top partners; they condense (again, in the chiral limit) according to $SU(3)_L \times SU(3)_R \to SU(3)_V$. In our model, the corresponding symmetry-breaking scheme is $SU(2)_L \times SU(2)_R \to SU(2)_V$. We believe that our model contains all the qualitative physics of Ferretti's model while offering a laboratory for developing quantitative techniques.

Multirep theories of physical significance are not easy to come by. Apart from the phenomenological requirements, Ferretti's choice of model is constrained [8] by the simple fact that higher-representation matter fields push gauge theories into the conformal window unless the number of fermions is quite small. It is essential that the gauge theory of hypercolor exhibit confinement and the concomitant breaking of global symmetries.

In this work we present results from the mesonic sector of the theory, leaving baryonic observables for another paper. We have already explored the mesonic and baryonic spectrum of the SU(4) gauge theories with only fundamental [9] or only sextet fermions [10].[2] Those results fit nicely into the body of work on QCD and its generalizations to larger values of N_c. The analysis there, similar to QCD studies, related the gauge coupling β and hopping parameter κ to a physical scale r_1 (the Sommer scale) and the quark mass m_q, and used the latter as an abscissa for plotting particle masses and decay constants. Here, of course, the space of bare couplings consists of the gauge coupling β and *two* hopping parameters κ_4 and κ_6 for the two fermion species. We translate these into the scale parameter t_0, derived from the Yang-Mills gradient flow, and the two quark masses m_4 and m_6.

Our main tool for understanding the meson spectrum is a recent generalization of chiral perturbation theory (χPT) to the low-energy sector of a two-representation theory [12]. This form of χPT provides formulas for masses, decay constants, and chiral condensates at next-to-leading order, with m_4 and m_6 as independent variables. These formulas contain an important qualitatively new piece of physics compared to QCD—communication between the different species. They describe, for instance, the dependence of the masses of the NG bosons of all the broken chiral symmetries on both fermion masses.

Another new feature of the two-representation theory is the existence of a nonanomalous singlet axial current, and a corresponding singlet NG boson that must be included in

the low-energy chiral theory. This particle is denoted ζ in Ref. [12] and is of significant phenomenological interest for composite Higgs models [8,13,14]. In this work we do not probe this singlet pseudoscalar state directly. Nevertheless we extract information about it indirectly, via its virtual contributions to the properties of the flavored NG bosons associated with chiral symmetry breaking of the individual representations. In particular, its decay constant in the chiral limit is a parameter in the chiral Lagrangian and thus appears as a fit parameter, allowing us to infer its mass using the leading-order formula.

Besides the pseudoscalar channel, we calculate masses and matrix elements of the lightest vector bosons. The vector is the lightest narrow resonance in QCD, and its properties are closely related to those of the pseudoscalars within the framework of vector meson dominance (VMD). We explore the evidence for VMD in our theory and its consequences for the decay width of the vector. This is of particular phenomenological interest, since in composite Higgs models, the vector resonance is often one of the first signatures expected in collider searches.

The paper is organized as follows. In Sec. II we describe the lattice theory, the observables we use, and ensembles we generated. In Sec. III we describe our application of χPT, including the discretization effects of Wilson fermions, and our scale-setting method which is based on t_0. In Sec. IV we present our results for the pseudoscalar spectrum and decay constants, including the flavor singlet ζ. We present the vector particles in Sec. V and use VMD to estimate decay widths. In Sec. VI we discuss our results from the point of view of large-N_c predictions, and present our overall conclusions.

The tables containing the various measured quantities have been collected together in Appendix A. In Appendix B we explain technical aspects of our analysis of lattice data. In Appendix C we review the definition of the U(1) axial current and of the mass parameter in Wilson χPT. Finally, Appendix D contains a calculation of perturbative Z-factors for the nHYP lattice action with dislocation suppression.

II. THE LATTICE THEORY

A. Symmetries

The chiral symmetry of the fundamental fermions and its expected breaking are the same as in two-flavor QCD. The specifics of chiral symmetry breaking for the sextet representation are less well known, so we will discuss them briefly; a more detailed explanation is given in [10,12].

The sextet representation of SU(4) is a real representation. Our model has two Dirac fermions charged under this representation, $\psi_i^{(6)}, \bar{\psi}_i^{(6)}, i = 1, 2$, which are equivalent to four Majorana fermions Ψ_I, $I = 1, \ldots, 4$. The global symmetry of the continuum theory is thus also SU(4). Using the language of Majorana fermions, the bilinear

---

[1]This scheme is not directly useful for model building since the SU(4)/SO(4) coset does not accommodate the Higgs field.

[2]A preliminary exploration of the chimera states—using configurations generated with only fundamental dynamical fermions—was presented in [11].

condensate $\langle \bar{\Psi}_I \Psi_J \rangle$ is symmetric in its Majorana-flavor indices. Hence, after spontaneous symmetry breaking one expects the unbroken symmetry to be SO(4) [15]. One consequence of the enlarged symmetry is that $\bar{\psi}^{(6)} \psi^{(6)}$ mesons and $\psi^{(6)} \psi^{(6)}$ diquarks (both gauge-singlet objects) are members of a degenerate multiplet of the unbroken group.

As usual, the chiral symmetries of the theory are explicitly broken by the Wilson term in the lattice action. The lattice theory thus has the same flavor symmetry as expected in the continuum theory after spontaneous symmetry breaking: $SU(2)_V \times U(1)_B$ for the fundamental representation and SO(4) for the sextet. Our use of Wilson fermions thus assumes that the spontaneous breaking of chiral symmetries is as would be forced by a bilinear condensate, and all measured correlation functions reflect this.

A special feature of the two-representation theory is the existence of a conserved U(1) axial current. While the individual U(1) currents $J_{5\mu}^{(4)}$ and $J_{5\mu}^{(6)}$ are anomalous, one can form a linear combination $J_{5\mu}$ of these currents that decouples from $F\tilde{F}$. Condensation of either fermion species then spontaneously breaks the nonanomalous axial symmetry, giving rise to a singlet NG boson that we denote ζ. We review the normalization of the U(1) current in Appendix C 1.

B. Lattice action and parameters

Our lattice action contains gauge-field terms and two fermion actions, one for each representation:

$$S = S_{\text{gauge}} + S_F^{(4)} + S_F^{(6)}. \qquad (2.1)$$

Each fermion action is a Wilson-clover action built of gauge links constructed by nHYP smearing [16,17]. In $S_F^{(6)}$ the smeared links are promoted to the sextet representation [10]. There are two hopping parameters, κ_4 and κ_6. We set both clover coefficients equal to unity, $c_{SW} = 1$, a choice known to work well with nHYP smearing in QCD [18] and with fermions in higher representations [19].

The gauge-field action takes the form

$$S_{\text{gauge}} = \beta S_{\text{plaq}} + \gamma S_{\text{NDS}}. \qquad (2.2)$$

The first term is the usual plaquette action, while the second is an nHYP dislocation-suppression (NDS) term [20], constructed from the nHYP-smeared links. The NDS term is designed to avoid singularities in the nHYP smearing. For the present study, we hold the ratio γ/β fixed at $1/125$ and use β as a free bare parameter.

Concurrent with the work described here, we are also studying the finite-temperature phase structure of the theory [21]. Comparison of the sextet-only limit of this theory to earlier published results [10] shows that the use of the NDS action removes the previously observed bulk transition from the interesting region of parameter space

(see also Ref. [22]). In the multirep theory, we see no evidence for a bulk transition anywhere near the range of bare parameters at which we run, indicating that all of our ensembles correspond to the confined continuum phase with broken chiral symmetry.

We extract masses and decay constants in the usual way from two-point correlation functions. We denote pseudo-scalar masses and decay constants in the representation r by M_{Pr} and F_{Pr}, respectively. The corresponding quantities in the vector channel are denoted by M_{Vr} and F_{Vr}.

We define the fermion masses m_4 and m_6 by imposing the axial Ward identity (AWI),

$$\partial_\mu \langle 0|A_{\mu a}^{(r)}(x)\mathcal{O}_r(0)|0\rangle = 2m_r \langle 0|P_a^{(r)}(x)\mathcal{O}_r(0)|0\rangle, \quad (2.3)$$

where $x \neq 0$, and a is an isospin index. We use the local unimproved axial current $A_{\mu a}^{(r)}$ and pseudoscalar density $P_a^{(r)}$ in each representation r. For the determination of the AWI mass, we do not renormalize these currents because the mass itself is not a physical observable; based on our perturbative renormalization of these currents described in Appendix D (used for calculation of decay constants), the effect of including the renormalization would be small anyway, amounting to a few-percent shift of the masses. For $\mathcal{O}_r$ we take a pseudoscalar source. When the distinction between representations is irrelevant, we will refer to the fermion mass defined by Eq. (2.3) as m_{AWI}. Further information about our conventions and methods for spectroscopy is given in Appendix B.

C. Scale setting

We set the scale in our simulations using the flow scale, t_0, introduced by Lüscher [23]. The flow scale is defined by the implicit equation

$$t^2\langle E(t)\rangle|_{t_0} = C, \qquad (2.4)$$

where $E(t) = \frac{1}{4}G_{\mu\nu}^a G_{\mu\nu}^a(t)$ is constructed from the clover form of the field strength $G_{\mu\nu}^a$ at flow time t. Here C is a dimensionless number, conventionally [23] taken to be 0.3 in QCD. With this choice, $\sqrt{t_0}$ corresponds to a length scale of 0.14 fm (i.e., an energy scale of 1.4 GeV) in QCD simulations [24,25].

For an arbitrary gauge theory, any value for C is *a priori* as good as any other. However, for comparison to existing studies with different gauge groups, it is useful to let C vary with N_c. Arguments from large-N_c QCD, supported by lattice data [25,26], suggest that $t_0 \sim N_c$ at leading order. For the SU(4) simulations of this work we therefore use

$$t^2\langle E(t)\rangle|_{t_0} = 0.3 \times \frac{4}{3} = 0.4. \qquad (2.5)$$

Lattice calculations give masses as dimensionless numbers Ma and gradient-flow scales as t_0/a^2. Dimensionless

products like $\hat{M} \equiv M\sqrt{t_0}$ eliminate the lattice spacing a, and our tables and figures will display such quantities. To aid the intuition, one can mentally convert $M\sqrt{t_0}$ to $M/(1.4\ \text{GeV})$.

We return to the subject of scale-setting and connect it to χPT in Sec. III below.

D. Ensembles

The ensembles used in this study are listed in Tables II–IV in Appendix A They fall into three groups. The short runs with the smallest lattices, of size $V = n_s^3 \times n_t = 16^3 \times 18$, were used for general orientation in the three-dimensional coupling space $(\beta, \kappa_4, \kappa_6)$. The most important observables for this step were $\sqrt{t_0}$, the scale defined by gradient flow (see Tables V–VII), and the masses M_{Pr} of the pseudoscalars constructed respectively from fermions in the $r = 4$ and 6 representations (see Tables VIII–X).

The goal of this orientation was to find couplings that give $t_0/a^2 = O(1)$ along with pseudoscalar masses that are reasonably light, for subsequent comparison to χPT. It turned out that these short runs yielded results that are in themselves usable for the chiral fits to be presented below, and hence we include them in our analysis.

As can be seen in the tables, some ensembles differ in small changes to their κ_r values. Our orientation runs found that t_0/a^2 and aM_P are often sensitive to these small changes.

We demanded that our ensembles satisfy the criterion $M_{Pr}L > 4$ for both representations, where $L = n_s a$ is the spatial size of the lattice. This is the familiar rule of thumb from QCD, based on the fact that leading-order finite-volume corrections are proportional to $e^{-M_\pi L}$; a more detailed study of finite-volume effects in our data is given in Appendix B 4. We considered cutting data above a maximum value of t_0/a^2 beyond which finite-volume effects severely contaminate determination of the flow scale; such a cut was found to be unnecessary following the cuts on $M_P L$. We did eliminate ensembles with $t_0/a^2 < 0.94$ because in these cases the flow did not enter a linear regime. These correspond to a large lattice spacing—in QCD language, $1/a < 1.3\ \text{GeV}$.

Having found interesting regions for study, we continued with high-statistics runs on lattices with $V = 16^3 \times 32$. Finally, we have four extended runs on lattices with $V = 24^3 \times 48$. These runs were done at large t_0/a^2 and small $\hat{M}_P$, so that the constraint $M_P L > 4$ demanded an increase in L/a.

The pseudoscalar masses for all the ensembles are given in Tables VIII–X. To show our coverage of M_P values, we map them in the (M_{P4}, M_{P6}) plane in Figs. 1 and 2. The first shows the pseudoscalar masses obtained for $0.94 < \sqrt{t_0}/a < 1.41$, which translates to a cutoff of
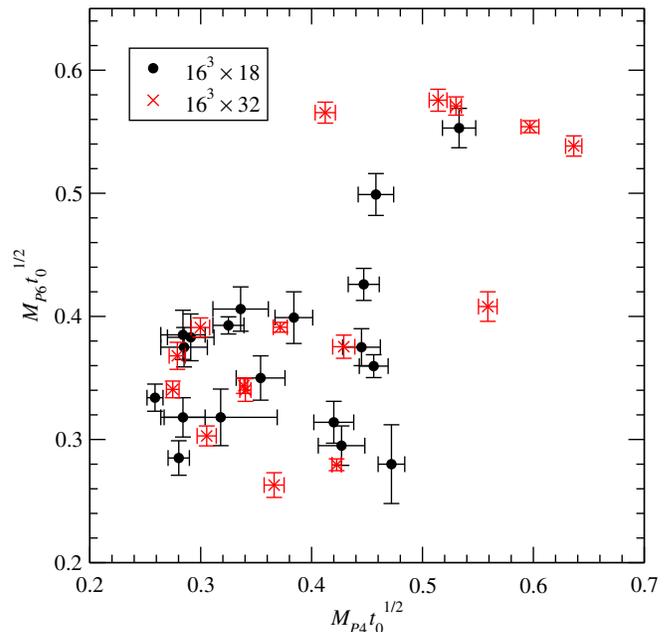
FIG. 1. Map of our ensembles in the plane of pseudoscalar masses M_{Pr}. These are coarse lattices, with $0.94 < \sqrt{t_0}/a < 1.41$. We define arbitrarily $\sqrt{t_0} = (1.4\ \text{GeV})^{-1}$ for comparison with QCD. For most of these ensembles $1/a \simeq 1.45\ \text{GeV}$ by this measure.

1.3 GeV $< 1/a < 2$ GeV in QCD language (most are in the neighborhood of $\sqrt{t_0}/a = 1.05$, or $1/a = 1.45$ GeV). The second plot represents ensembles in the range $1.41 < \sqrt{t_0}/a < 1.64$, or 2 GeV $< 1/a < 2.3$ GeV.
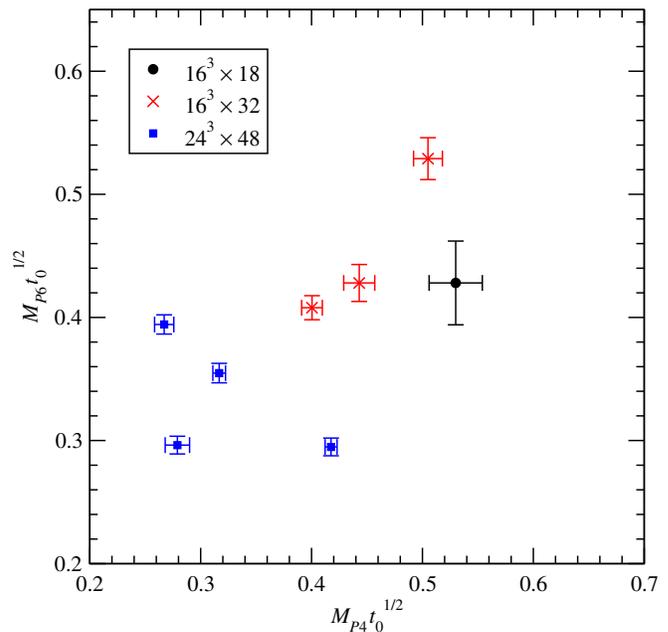
FIG. 2. Same as Fig. 1, but here we plot ensembles on fine lattices, $\sqrt{t_0}/a > 1.41$. If we fix $\sqrt{t_0} = (1.4\ \text{GeV})^{-1}$ then this means $1/a > 2$ GeV. The blue squares are all at $1/a \simeq 2.1$ GeV.

III. CHIRAL PERTURBATION THEORY

The standard framework for analyzing the light pseudoscalar sector is χPT. The generalization of χPT to a theory with fermions in two different representations was developed in Ref. [12], and the next-to-leading-order (NLO) results of this work provide the basis for our fits for the pseudoscalar masses and decay constants. We will also need Wilson chiral perturbation theory (WχPT), the extension of chiral perturbation theory to include the discretization errors of Wilson fermions [27–32].

A. Using a yardstick

We need a yardstick with which to measure dimensionful quantities as the fermion masses are varied. In this paper, we use $\sqrt{t_0}$ for the characteristic length scale of every ensemble. To measure an observable in units of t_0 simply means to multiply it by the power of t_0 that renders it dimensionless. Since t_0 itself admits a chiral expansion [33], the resulting dimensionless quantity admits a chiral expansion whenever the original dimensionful observable does.

To see how this works, consider a gauge theory with mass-degenerate fermions of mass m, all in the same representation. In continuum χPT, the NLO expression for the decay constant is

$$F^{\text{NLO}} = F\left(1 + c\frac{2Bm}{8\pi^2 F^2}\log\left(2Bm/\mu^2\right) + L\frac{2Bm}{F^2}\right). \quad (3.1)$$

B and F are the familiar parameters of the LO lagrangian. [Our normalization convention for the pseudoscalar decay constant is larger by $\sqrt{2}$ than that commonly used in the χPT literature. See Eq. (4.1) below.] We recall that the LO pseudoscalar mass is

$$(M^2)^{\text{LO}} = 2Bm. \quad (3.2)$$

The remaining parameters in Eq. (3.1) are μ, the renormalization scale, and L, which is a (dimensionless) linear combination of the NLO low-energy constants (LECs), whose value depends on the choice of μ. The coefficient c of the logarithmic term is a calculable number that depends only on the fermion representation and on the number of flavors [34].

The NLO result for t_0 is

$$t_0^{\text{NLO}} = t_{0,\text{ch}}\left(1 + \tilde{k}_1\frac{2Bm}{F^2}\right), \quad (3.3)$$

where $t_{0,\text{ch}}$ is the value of t_0 in the chiral limit, and $\tilde{k}_1$ is a new LEC. Notice that this expression depends analytically on the fermion mass m. As was shown in Ref. [33], logarithmic corrections to t_0 occur for the first time at the next-to-next-to-leading order (N²LO).

Combining Eqs. (3.1) and (3.3) we obtain the NLO result for the dimensionless product $\hat{F} \equiv F\sqrt{t_0}$,

$$\hat{F}^{\text{NLO}} = F\sqrt{t_{0,\text{ch}}}\left(1 + c\frac{2Bm}{8\pi^2 F^2}\log(2Bmt_0)\right.$$
$$\left. + (L + \tilde{k}_1/2)\frac{2Bm}{F^2}\right). \quad (3.4)$$

Here we have chosen the renormalization scale to be $\mu = t_{0,\text{ch}}^{-1/2}$. LECs are independent of the fermion mass, and to preserve this feature we rescale them with $t_{0,\text{ch}}$, for example defining $\mathring{F} = F\sqrt{t_{0,\text{ch}}}$. Equation (3.4) can then be written as

$$\hat{F}^{\text{NLO}} = \mathring{F}\left(1 + c\frac{2\mathring{B}\,\mathring{m}}{8\pi^2 \mathring{F}^2}\log(2\mathring{B}\,\mathring{m}) + (L + \tilde{k}_1/2)\frac{2\mathring{B}\,\mathring{m}}{\mathring{F}^2}\right). \quad (3.5)$$

The expansion parameter is now $\mathring{m}$, which is the fermion mass m measured in units of $t_{0,\text{ch}}$.

Equation (3.5) is inconvenient because $\mathring{m}$ is not known for a given ensemble until $t_{0,\text{ch}}$ is known. Finding $t_{0,\text{ch}}$ (in units of t_0 of the given ensemble) requires a complicated fitting procedure that we wish to avoid. Instead, we opt for rescaling all observables of a given ensemble, including the fermion mass, with t_0 of the same ensemble. Introducing $\hat{m} \equiv m\sqrt{t_0}$ we now use Eq. (3.3) to relate the rescaled masses,

$$\mathring{m} = \hat{m}\left(1 - \tilde{k}_1\frac{Bm}{F^2}\right), \quad (3.6)$$

which allows us rewrite Eq. (3.5) as

$$\hat{F}^{\text{NLO}} = \mathring{F}\left(1 + c\frac{2\mathring{B}\,\hat{m}}{8\pi^2 \mathring{F}^2}\log(2\mathring{B}\,\hat{m}) + (L + \tilde{k}_1/2)\frac{2\mathring{B}\,\hat{m}}{\mathring{F}^2}\right). \quad (3.7)$$

The transition from $\mathring{m}$ to $\hat{m}$ left no trace, because the difference is a higher-order correction. More generally, at NLO the transition from $\mathring{m}$ to $\hat{m}$ can always be absorbed into a redefinition of the LECs. (A case where the redefinition is nontrivial is the NLO result for the pseudoscalar mass.)

An appealing feature of Eq. (3.7) is that it looks the same as Eq. (3.1). In particular, the coefficient of the logarithmic term is unchanged. The only minor change is that the coefficient of the NLO analytic term is now $L + \tilde{k}_1/2$ instead of L. (At N²LO things would become technically more complicated, because N²LO logarithmic corrections

for t_0 would have to be incorporated as well.) It can be checked that this nice feature generalizes to an arbitrary fermion content. In the NLO fit formulas that we present below, all the logarithmic terms will thus have the same coefficients as in the usual continuum NLO expressions [12,34].

B. Wilson chiral perturbation theory

The extension of continuum chiral perturbation theory to include the discretization errors of Wilson fermions goes under the name of Wilson chiral perturbation theory, or WχPT. In the light pseudoscalar sector, WχPT allows us to extrapolate both to the chiral limit, $m \to 0$, and to the continuum limit, $a \to 0$. WχPT comes in two variants, depending on the choice of a power-counting scheme. In this paper we follow the "generic small mass," or GSM, power counting, defined by

$$p^2 \sim m \sim a, \qquad (3.8)$$

where p is an external momentum, m is the fermion mass, and a is the lattice spacing, all measured in terms of a typical hadronic scale. The alternative power-counting scheme, known as the "large cutoff effects," or LCE, power counting, is defined by

$$p^2 \sim m \sim a^2. \qquad (3.9)$$

The GSM scheme is appropriate when the fermion mass is not too small, and $O(a^2)$ effects may be considered as subleading corrections. (We must, of course, remain within the chiral regime, meaning that $\hat{m} = m\sqrt{t_0}$ is small.) In particular, our determination of the critical surface κ_r^c, where the mass of fermions in representation r vanishes, is done via extrapolation from the GSM regime. As a result, we do not probe the possible existence of an Aoki phase. For more details, see Appendices B 3 and C 2.

The fermion mass appearing in the LO Lagrangian of WχPT is the so-called *shifted mass*, defined by

$$m_{\text{shifted}} = m_{\text{ctm}} + aW_0/B, \qquad (3.10)$$

where m_{ctm} is the fermion mass of continuum χPT, and W_0 is a new LEC from WχPT. The difference between the shifted and continuum masses vanishes in the continuum limit. For this lattice study, we need to know how the shifted mass m_{shifted} compares to the fermion mass m_{AWI} measured in our simulations via the axial Ward identity Eq. (2.3). As was shown in Ref. [35], $m_{\text{shifted}} = m_{\text{AWI}}$, up to corrections that are higher order in either of the above power-counting schemes. In view of the important role that this result plays in our analysis, we briefly summarize the derivation of Ref. [35] in Appendix C 2. For our chiral fits we thus define

$$\hat{m} = m_{\text{AWI}}\sqrt{t_0}. \qquad (3.11)$$

The last ingredient we need for our fits is the lattice spacing. Since we are measuring all dimensionful quantities in units of t_0, it is natural to adopt a *mass-dependent* prescription, and to measure also the lattice spacing in units of t_0. We thus introduce

$$\hat{a} \equiv a/\sqrt{t_0}. \qquad (3.12)$$

The Wilson discretization effects of any hatted (dimensionless) observable will be accounted for by an expansion in $\hat{a}$.

In QCD, it is common to choose a *mass-independent* scale-setting prescription, whereby the lattice spacing is a function of the bare coupling β, but is independent of the bare fermion masses (see for example Refs. [36,37]). In brief, for every constant-β plane, this procedure requires finding the point where certain dimensionless quantities (such as M_π/F_π and M_K/F_K) attain their real-world values. The value in lattice units of some dimensionful observable at the reference point is then used to determine the lattice spacing in physical units.

Here we have opted for mass-dependent scale setting because of several important differences. First, the BSM context does not provide us with any experimental results that could be used to define a reference point. This problem might be circumvented by invoking the chiral limit as a reference point on each constant-β plane. This, however, has the undesirable feature that the scale-setting procedure would necessarily involve an extrapolation.

Second, in our model, as in many other models that have been studied in the BSM context, we observe a rapid change of t_0/a^2 with the fermion mass, especially when the latter becomes light. Moreover, this phenomenon is quite general, and is seen for virtually any quantity that might be used to set the scale; its proper interpretation is thus that the lattice spacing itself is changing rapidly. The underlying reason is that, in comparison with QCD, BSM theories tend to have a large number of fermionic degrees of freedom, which have a strong screening effect on the bare coupling. When we consider the dependence of a hatted quantity, such as $\hat{M}_P$, on the hatted mass parameter, $\hat{m}$, we expect to see some deviations from the continuum values, but such scaling violations should be small when the bare coupling is small enough. By contrast, as explained above, the lattice spacing $\hat{a}$ itself can vary rapidly with the fermion mass(es). By using the mass-dependent scale-setting prescription of Eq. (3.12) we can incorporate this effect into our analysis. As we will see, the remaining scaling violations in the hatted quantities are small and amenable to WχPT.

C. Summary of χPT formulae

Our central fits below will include terms through NLO in the GSM power counting. These formulas depend exclusively on the dimensionless quantities we have introduced

in the previous subsections. The NLO expressions for the pseudoscalar masses of the two representations are

$$(\hat{M}_{P4}^2)^{\mathrm{NLO}} = 2\hat{m}_4 \mathring{B}_4 \left(1 + L_{44}^M \hat{m}_4 + L_{46}^M \hat{m}_6 + \frac{1}{2}\Delta_4 - \frac{4}{5}\Delta_\zeta \right)$$
$$+ \mathring{W}_{44}^M \hat{a}\hat{m}_4 + \mathring{W}_{46}^M \hat{a}\hat{m}_6 + \mathring{W}_4^M \hat{a}^2, \qquad (3.13)$$

$$(\hat{M}_{P6}^2)^{\mathrm{NLO}} = 2\hat{m}_6 \mathring{B}_6 \left(1 + L_{66}^M \hat{m}_6 + L_{64}^M \hat{m}_4 - \frac{1}{4}\Delta_6 - \frac{1}{5}\Delta_\zeta \right)$$
$$+ \mathring{W}_{66}^M \hat{a}\hat{m}_6 + \mathring{W}_{64}^M \hat{a}\hat{m}_4 + \mathring{W}_6^M \hat{a}^2, \qquad (3.14)$$

while the expressions for the decay constants are

$$(\mathring{F}_{P4})^{\mathrm{NLO}} = \mathring{F}_4(1 + L_{44}^F \hat{m}_4 + L_{46}^F \hat{m}_6 - \Delta_4) + \mathring{W}_4^F \hat{a}, \quad (3.15)$$

$$(\mathring{F}_{P6})^{\mathrm{NLO}} = \mathring{F}_6(1 + L_{66}^F \hat{m}_6 + L_{64}^F \hat{m}_4 - 2\Delta_6) + \mathring{W}_6^F \hat{a}. \quad (3.16)$$

The one-loop chiral logarithms enter as

$$\Delta_4 = \frac{2\hat{m}_4 \mathring{B}_4}{8\pi^2 \mathring{F}_4^2} \log(2\hat{m}_4 \mathring{B}_4),$$

$$\Delta_6 = \frac{2\hat{m}_6 \mathring{B}_6}{8\pi^2 \mathring{F}_6^2} \log(2\hat{m}_6 \mathring{B}_6),$$

$$\Delta_\zeta = \frac{\hat{M}_\zeta^2}{8\pi^2 \mathring{F}_\zeta^2} \log(\hat{M}_\zeta^2), \qquad (3.17)$$

where the dimensionless mass-squared of the singlet NG boson is *defined* by

$$\hat{M}_\zeta^2 = \frac{8}{5} \left(\frac{2\mathring{F}_4^2 \hat{m}_4 \mathring{B}_4 + \mathring{F}_6^2 \hat{m}_6 \mathring{B}_6}{\mathring{F}_\zeta^2} \right). \qquad (3.18)$$

This corresponds to the LO result of Ref. [12], rescaled by t_0. Further technical details related to the ζ and our conventions for the conserved axial current appear in Appendix C 1.

The most important parameters in the expressions above are the LO LECS of the continuum two-representation theory (rescaled by $\sqrt{t_{0,\mathrm{ch}}}$): $\mathring{B}_4$, $\mathring{B}_6$, $\mathring{F}_4$, $\mathring{F}_6$, and $\mathring{F}_\zeta$. The dimensionless parameters L_{rs}^M and L_{rs}^F, $r = 4, 6$, are linear combinations of the continuum NLO LECs and of similar NLO LECs originating from the chiral expansion of the flow scale [cf. Eq. (3.3)]. The general form of the analytic NLO continuum terms was discussed in [12]. Because we do not have enough independent quantities to distinguish the individual NLO LECs, we instead consider L_{rs}^M and L_{rs}^F as the parameters for the fit. Finally, the various $\mathring{W}$ parameters account for the NLO analytic terms of WχPT in the GSM power-counting scheme. Overall, these

formulas contain 21 undetermined parameters, which we will fit below using 172 correlated points of data: four data points for each of our 43 ensembles.

We have not presented NLO fit formulas for the mass and decay constant of the singlet NG boson ζ. We do not make use of these formulas in this work because we have not calculated fermion-disconnected diagrams, which is technically challenging, and so we do not have direct access to the singlet sector. Nevertheless, through their dependence on Δ_ζ, virtual ζ loops contribute to the masses and decay constants of the other NG bosons at NLO. In the next section we will explore what can be learned about the singlet sector from this effect.

Another interesting quantity is the chiral condensate in each representation. At lowest order in χPT (equivalently, in the corresponding chiral limit, $\hat{m}_r \to 0$), the fermion condensate per flavor is given by

$$\hat{\Sigma}_r = -\mathring{B}_r \mathring{F}_r^2. \qquad (3.19)$$

Instead of measuring the condensates directly—a formidable task with Wilson fermions—we will make use of Eq. (3.19) to extract their values in the (double) chiral limit from our analysis of the pseudoscalar masses and decay constants.

IV. PSEUDOSCALAR MESONS

A. Masses and decay constants

We begin with the pseudoscalar mesons, which become NG bosons in the chiral limit. For a first look, we plot in Fig. 3 the squared masses $\hat{M}_{Pr}^2$. The sextet mass $\hat{M}_{P6}$ is plotted against the AWI mass $\hat{m}_6$ of the sextet fermion, ignoring the dependence on the fundamental fermion mass $\hat{m}_4$, and likewise for $\hat{M}_{P4}$, plotted against $\hat{m}_4$. As expected from leading-order chiral perturbation theory, the overall
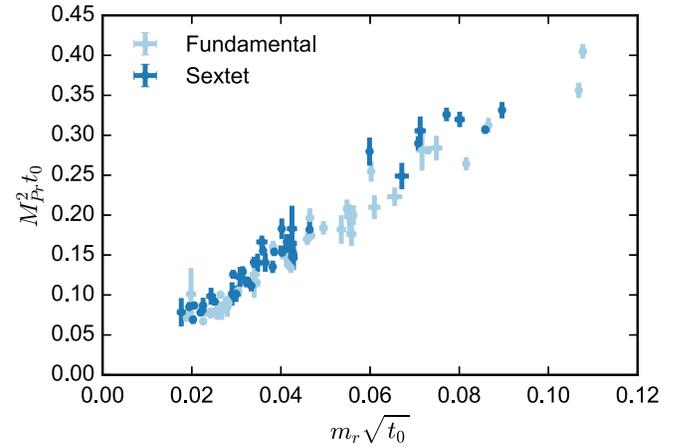
FIG. 3. Squared mass of the two pseudoscalar species, each plotted against the AWI mass of the corresponding fermion species, all in units of the flow scale t_0.

behavior of each squared mass is approximately linear. One supposes that the scatter around the straight lines is due to the hidden dependence on the other fermion mass, as well as corrections from NLO and from lattice artifacts. We will examine this hypothesis shortly.

The pseudoscalar decay constants are defined by

$$\langle 0|A_{4a}^{(r)}|P_b^{(r)}\rangle = \delta_{ab}M_{Pr}F_{Pr}, \qquad (4.1)$$

at zero spatial momentum, which is the convention that gives $F_\pi \simeq 130$ MeV in QCD. We calculate F_{Pr} with the procedure described in Appendix B 2, renormalizing according to the analog of Eq. (B5). We plot the (rescaled) decay constants $\hat{F}_{Pr}$ in Fig. 4. The data show a steady rise with $\hat{m}_r$. The same qualitative behavior is seen in QCD, where the pion decay constant is an increasing function of the quark mass.

We have presented in Sec. III C the predictions of χPT in NLO for pseudoscalar observables. We conduct a joint fit of the four observables $\hat{M}_{Pr}^2$ and $\hat{F}_{Pr}$ to the NLO formulas of Eqs. (3.13)–(3.16). On each ensemble, we use single-elimination jackknife to construct the 6×6 correlation matrix among pseudoscalar masses, decay constants, and AWI masses of the fermions. These correlation matrices enter into the χ^2 that is minimized for the fit. We do not include correlations with the flow scale t_0, which has negligible error compared to the other quantities we extract.

The full NLO fit to 21 parameters and $172 - 21 = 151$ degrees of freedom gives $\chi^2/\text{DOF} = 0.48$. Table I contains the resulting values for the LECs and demonstrates the presence of important lattice artifacts in our data. For the masses, the most significant terms are the $\mathcal{O}(\hat{m}_r\hat{a})$ artifacts, in the same representation. For the decay constants, the $\mathcal{O}(\hat{a})$ artifacts are also significant. From an empirical perspective, these four NLO Wilson terms form a necessary minimal set of artifact terms for modeling the data.
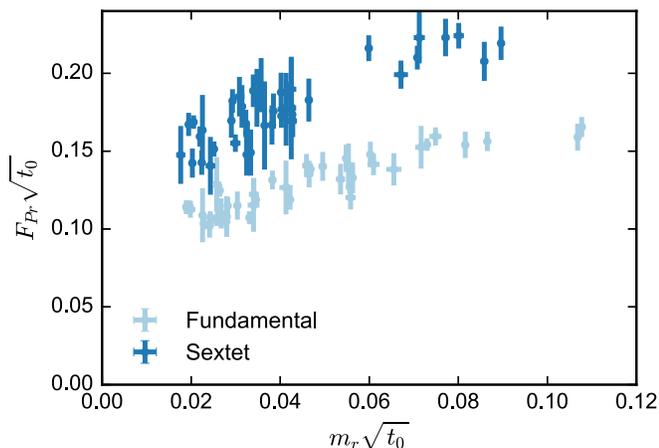
FIG. 4. Decay constant of each pseudoscalar species plotted against the mass of the corresponding fermion species, in units of the flow scale t_0.

TABLE I. Parameter values from a joint fit to the full NLO χPT formulas.

LO:	$\mathring{B}_4$	2.4(2)
	$\mathring{B}_6$	2.7(1)
	$\mathring{F}_4$	0.114(7)
	$\mathring{F}_6$	0.17(1)
	$\mathring{F}_\zeta$	0.16(2)
Continuum NLO:	L_{44}^F	3.4(5)
	L_{46}^F	1.4(6)
	L_{64}^F	0.3(4)
	L_{66}^F	3.9(5)
	L_{44}^M	0.1(7)
	L_{46}^M	3.(1)
	L_{64}^M	0.4(7)
	L_{66}^M	0.5(7)
Lattice NLO:	$\mathring{W}_4^F$	$-0.055(6)$
	$\mathring{W}_6^F$	$-0.08(1)$
	$\mathring{W}_4^M$	0.01(1)
	$\mathring{W}_{44}^M$	$-1.9(3)$
	$\mathring{W}_{46}^M$	$-0.6(3)$
	$\mathring{W}_6^M$	0.001(9)
	$\mathring{W}_{64}^M$	0.1(2)
	$\mathring{W}_{66}^M$	$-2.5(4)$

Figures 5 and 6 illustrate the sizes of the Wilson artifacts (red) emerging from this fit. In these figures, the "corrected" data (dark blue) result from subtracting the lattice artifacts from the data (light blue), allowing us to extrapolate to the continuum limit, $\hat{a} \to 0$. The corrected data follow fairly well the tree-level formula for the pseudoscalar masses and the continuum NLO result for the decay constants, respectively, both indicated by green bands. (The bands represent 1σ in the fit parameters.) In order to display a smooth curve for the continuum NLO result for the decay constants, we have included only the same-representation terms when drawing the green band (indicated by "continuum NLO SREP" in the figure). The remaining scatter and deviation in the subtracted data (dark blue) is evidence of coupling between the representations.

Table I demonstrates that all five leading-order LECs are well determined by the NLO fit. We note that the singlet decay constant $\mathring{F}_\zeta$ is larger than $\mathring{F}_4$ and similar in size to $\mathring{F}_6$. Because measurement of chiral logarithms is known to be a difficult task in QCD studies, we return to the question of the stability of this result below.
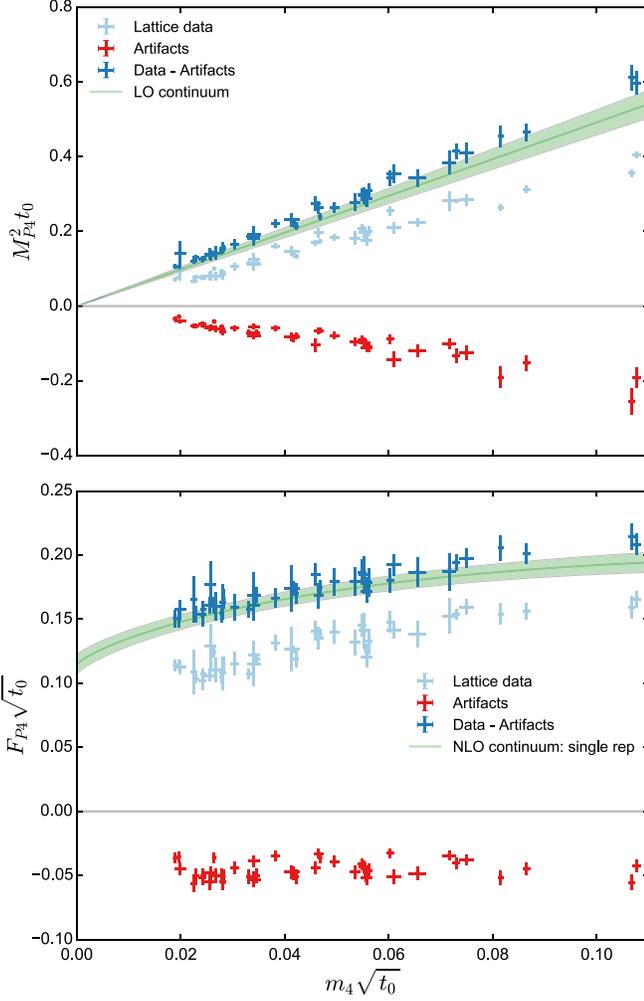
FIG. 5. Breakdown of the contribution of lattice artifacts in the joint fit to χPT for the fundamental masses and decay constants.

FIG. 6. Breakdown of the contribution of lattice artifacts in the joint fit to χPT for the sextet masses and decay constants.

Turning our attention to the NLO LECs, we examine the communication between the representations. The ratios L_{46}^M/L_{44}^M and L_{46}^F/L_{44}^F quantify the relative influence of the sextet fermions on $\hat{M}_{P4}^2$ and $\hat{F}_{P4}$, respectively, in the continuum theory. Similarly, the ratio $\mathring{W}_{46}^M/\mathring{W}_{44}^M$ measures the relative influence of the sextet artifact term compared to the fundamental artifact term in $\hat{M}_{P4}^2$. Taking into account correlations, the following ratios are different from zero at the 2σ level:

$$L_{46}^F/L_{44}^F = +0.4(2), \qquad (4.2)$$

$$\mathring{W}_{46}^M/\mathring{W}_{44}^M = +0.30(15). \qquad (4.3)$$

The converse influence of the fundamentals upon the sextets follows from exchanging (4⇌6). The ratios L_{64}^M/L_{66}^M, L_{64}^F/L_{66}^F, and $\mathring{W}_{64}^M/\mathring{W}_{66}^M$ are all consistent with zero. Despite the large uncertainties, this suggests that the

sextets influence the fundamentals significantly, while the converse is not true. The same qualitative conclusion is also evident, for instance, in the NLO continuum behavior of the decay constants. Figure 6 shows that subtracted data (dark blue) are, to good approximation, a smooth function of $\hat{m}_6$ only. In contrast, the corresponding fundamental result in Fig. 5 (also in dark blue) exhibits a conspicuous jaggedness, indicating important dependence on the sextet fermion mass.

B. Stability of the NLO fit

In this subsection we explore the stability of the NLO fit. First, since we are using priors to ensure convergence of the nonlinear fitting procedure, it is important to verify that our results were not biased by them. To this end, we have redone the fit using the results of the first fit as initial guess, while multiplying the width of all priors by 10. Figure 7 shows the results of both fits for the 5 LO LECs in the two lines at the bottom. The results are indistinguishable,
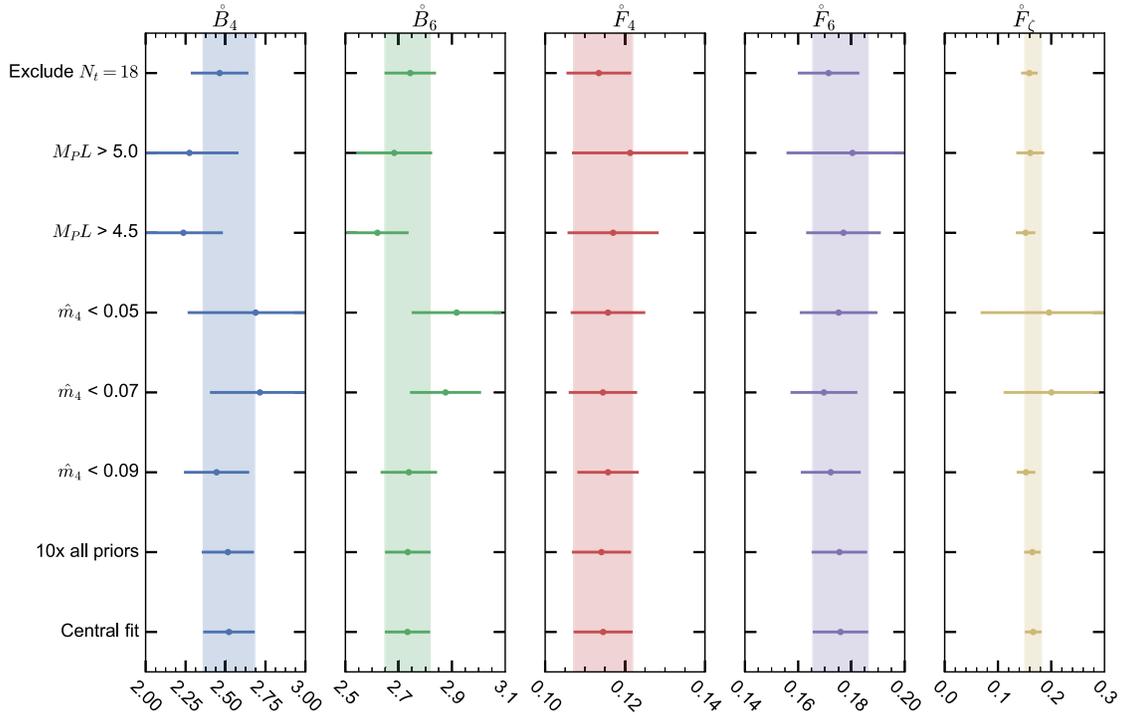
FIG. 7.   Exploring the stability of leading-order LECs in chiral fits. We take the NLO result to define our central values, which appear at the bottom of each column. The variations are described in the text.

indicating that the LO LECs were not influenced by the priors. (The same is also true for the NLO LECs.)

The chiral fit provides *a posteriori* justification for the use of the GSM power-counting scheme, where $\mathcal{O}(a^2)$ terms are not part of the LO lagrangian. Both fermion masses in our ensembles lie roughly in the range

$$0.02 \lesssim \hat{m}_r \lesssim 0.10. \qquad (4.4)$$

The range of lattice spacings we explore is

$$0.4 \lesssim \hat{a}^2 \lesssim 1.1. \qquad (4.5)$$

[Recall that our scale setting implies $\hat{a}^2 = a^2/t_0$ by definition; see Eq. (3.12).] The $\mathcal{O}(m_r)$ contribution to the pseudoscalar masses is $2\mathring{B}_r\hat{m}_r$, while the $\mathcal{O}(a^2)$ contribution is $\mathring{W}_r^M \hat{a}^2$. For our fermion masses and lattice spacings, these contributions lie approximately within the following ranges:

$$2\mathring{B}_r\hat{m}_r: \ 5 \times [0.02, 0.1] \approx [0.1, 0.5], \qquad (4.6)$$

$$\mathring{W}_r^M \hat{a}^2: \ 0.01 \times [0.4, 1.1] \approx [0.004, 0.01]. \qquad (4.7)$$

We see that the $\mathcal{O}(m_r)$ terms are at least an order of magnitude larger than the $\mathcal{O}(a^2)$ terms, showing that the

GSM power counting is the appropriate one (as long as this picture is not upset by large N^2LO corrections, see below).

Measurement of the LECs also provides information about the convergence of the chiral expansion. With our convention for the decay constant, the expansion parameters of continuum χPT are $\xi_r \equiv 2\mathring{B}_r\hat{m}_r/8\pi^2\mathring{F}_r^2$. With the central-fit values for the LECs, these fermion masses correspond to the following ranges for the expansion parameters:

$$0.09 \lesssim \xi_4 \lesssim 0.50, \qquad (4.8)$$

$$0.04 \lesssim \xi_6 \lesssim 0.20. \qquad (4.9)$$

We see that the maximum of the sextet expansion parameter ξ_6 is smaller by a factor of 2.5 than the fundamental expansion parameter ξ_4. The main reason is that $\mathring{F}_6$ is significantly larger than $\mathring{F}_4$, as might be expected based on the relative dimension of the two representations (see Sec. VI A).

It is quite plausible that ξ_6 is sufficiently small that the expansion in m_6 converges well over our entire ensemble set. The same may not be true for ξ_4, whose value can be as large as 0.5. In the next three lines of Fig. 7 we study the influence on the LO LECs of dropping ensembles at the high end of the $\hat{m}_4$ range: $\hat{m}_4 > 0.09$, >0.07, and finally >0.05. We see that truncating our data set has only a

modest effect on the $\mathring{F}_r$ and $\mathring{B}_r$ parameters. On the other hand, since we only obtain $\mathring{F}_\zeta$ through NLO logarithms, it is not surprising that the increase in the error bar of $\mathring{F}_\zeta$ is much more pronounced. Indeed, when we restrict to $\hat{m}_4 < 0.05$, $\mathring{F}_\zeta$ is only 2σ away from zero.

The next two lines in Fig. 7 investigate the possible influence of finite-volume effects on our central analysis; further discussion appears in Appendix B 4. The minimum cutoff on $M_P L$ in data used in the central fit is varied from its initial value of 4.0 in our main analysis to 4.5 and 5.0, excluding more data which would be expected to have the largest finite-volume contamination. Finally, in the top line we repeat our fit with all $V = 16^3 \times 18$ ensembles excluded from the analysis, in order to test for systematic effects in our correlator analysis due to the smaller time extent. No significant change to our results is seen in any case.

The main systematic uncertainty about this non-QCD system is the neglect of N^{2}LO corrections. We do not really know how high can we go in ξ_4 and ξ_6 if we want these corrections to remain below a certain level. While our stability tests give us some insight, we do not have enough data for a quantitative study of N^{2}LO. Nevertheless, we take the smallness of ξ_6 and our stability tests on $\hat{m}_4$ as evidence that the data are in the regime where NLO ChPT applies, even if we do not have enough information to quantify the corresponding systematic error.

C. The singlet Goldstone boson ζ

As explained in Sec. III C, the chiral fit in the fundamental and sextet sectors allows us to probe the ζ meson as well. We examine its mass in the chiral-sextet limit, $\hat{m}_6 \to 0$. Figure 8 shows $\hat{M}_\zeta^2$, constructed using Eq. (3.18) and the parameters
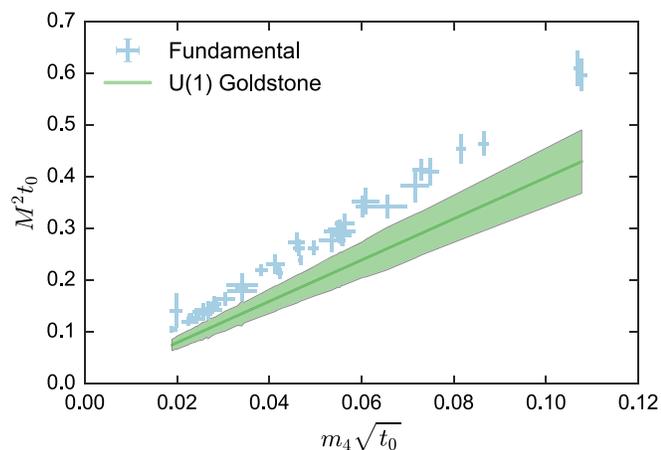
FIG. 8. Mass squared $\hat{M}_\zeta^2$ of the nonanomalous NG boson in the combined continuum ($\hat{a} \to 0$) and chiral-sextet ($\hat{m}_6 \to 0$) limits, as extracted using Eq. (3.18) and the central fit's parameters, plotted against $\hat{m}_4$. The pseudoscalar mass $\hat{M}_4^2$ in the fundamental sector in the same limit is shown for comparison.

of the central fit, in the continuum ($\hat{a} \to 0$) limit, as a function of the mass $\hat{m}_4$ of the fundamental fermions. The figure shows that the singlet boson is consistently lighter than the pseudoscalar of the fundamental sector in this limit.

We can make a conservative prediction regarding the ζ mass as follows. As we have just explained, we do not know how large $\hat{m}_4$ can be while keeping the N^{2}LO corrections below, say, 10% or 20%. Lowering the maximal value of $\hat{m}_4$ raises the uncertainty in $\mathring{F}_\zeta$, as seen in Fig. 7. Still, even if we lower the maximal value of $\hat{m}_4$ so as to, say, double the uncertainty of $\mathring{F}_\zeta$, we would still find that $M_\zeta^2 < M_4^2$ at the 1σ level.

The chiral-sextet limit is interesting for composite-Higgs models. In many models, including those proposed by Ferretti and Karateev [8], the symmetries of the Standard Model are embedded into the unbroken global symmetries, so that neither the fundamental nor the sextet fermions are required to be strictly massless. Nonetheless, successful models are likely to have very light sextet fermions, because a large sextet mass would prevent the Higgs field from condensing even after the generation of a potential from the coupling of the Higgs to Standard Model fields.

V. VECTOR MESONS

A. Masses and decay constants

We now turn to our results for vector masses and decay constants. Vector-meson decay constants appear in the literature with a variety of conventions. We define F_{Vr} to have units of energy,

$$\langle 0 | V_{ia}^{(r)} | V_{jb}^{(r)} \rangle = \delta_{ab} \delta_{ij} F_{Vr} M_{Vr}, \qquad (5.1)$$

where the vector meson is at rest. The indices are $i, j = 1, 2, 3$, for the spatial directions, and as usual, $a, b = 1, 2, 3$, for isospin. This definition is frequently used in the phenomenology literature on precision electroweak observables, for example Ref. [38].

Figures 9 and 10 show results for $\hat{M}_{Vr}$ and $\hat{F}_{Vr}$, respectively, each plotted against the fermion mass $\hat{m}_r$ in the same representation. As before, we measure all quantities in units of t_0. The data for these plots are listed in Tables XI–XIII. Both quantities shows a modest, plausibly linear rise against the fermion mass, albeit with a large spread.

Figure 11 shows the ratio of the pseudoscalar and vector masses, M_{Pr}/M_{Vr}, again plotted against the fermion mass $\hat{m}_r$ in the same representation. This ratio is greater than or equal to a half for all but the smallest masses. Because the decay $V \to PP$ is p-wave, the vector is stable if $M_P/M_V > 0.5\sqrt{1 - 4k_{\min}^2/M_V^2}$, where $k_{\min} = 2\pi/L$ is the minimum nonzero momentum. This condition is satisfied for both representations on all of our ensembles, so the vectors are indeed stable.
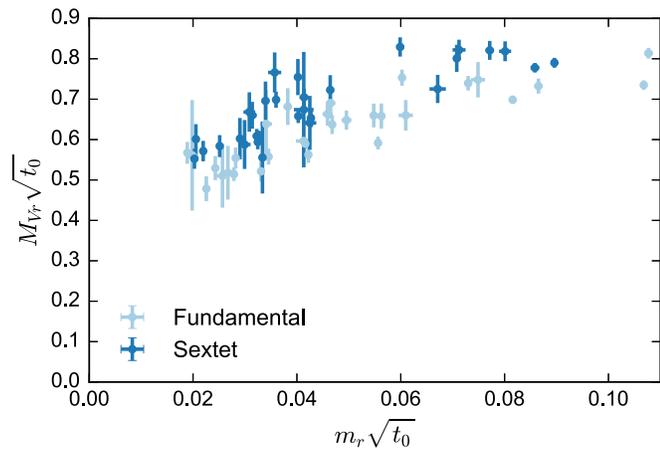
FIG. 9. Vector masses vs fermion masses in units of the flow scale t_0.
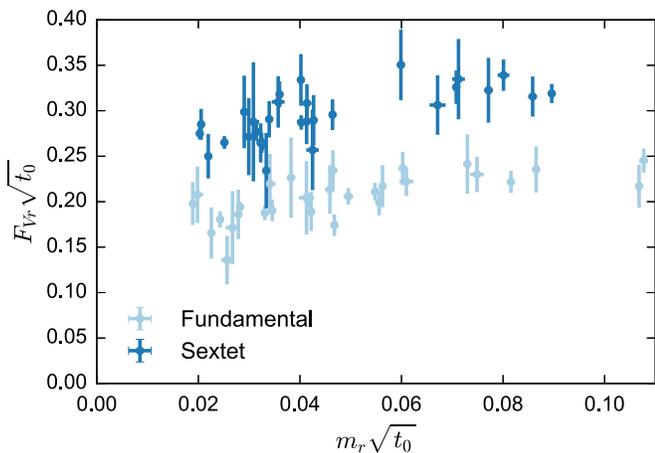
FIG. 10. Vector decay constants vs fermion masses in units of the flow scale t_0.
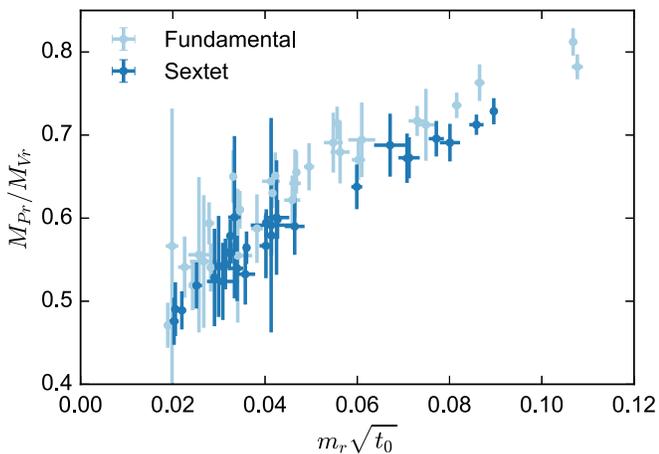
FIG. 11. The mass ratio M_{Pr}/M_{Vr} in a fixed representation.

We model $\hat{M}_{Vr}$ and $\hat{F}_{Vr}$ as linear functions of the fermion mass in the same representation and of the lattice spacing, for example,

$$\hat{M}_{V4} = c_0 + c_1\hat{m}_4 + c_2\hat{a}. \qquad (5.2)$$

For this analysis, we restrict ourselves to the 30 ensembles for which we were able to measure the vector decay constants (see Tables XI–XIII). The individual correlated fits are successful, with typical $\chi^2/\text{DOF} \lesssim 1.0$ for $30 - 3 = 27$ degrees of freedom. Figures 12 and 13 illustrate the contribution of lattice artifacts to these fits in the same manner as for the pseudoscalars above; the green bands represent the linear continuum terms in each fit.

B. Vector meson dominance and the KSRF relations

The pseudoscalar and vector decay constants are related through the hypothesis of vector meson dominance (VMD). Kawarabayashi, Suzuki, Riazuddin, and Fayyazuddin (KSRF) showed long ago [39–41] that VMD leads to the prediction
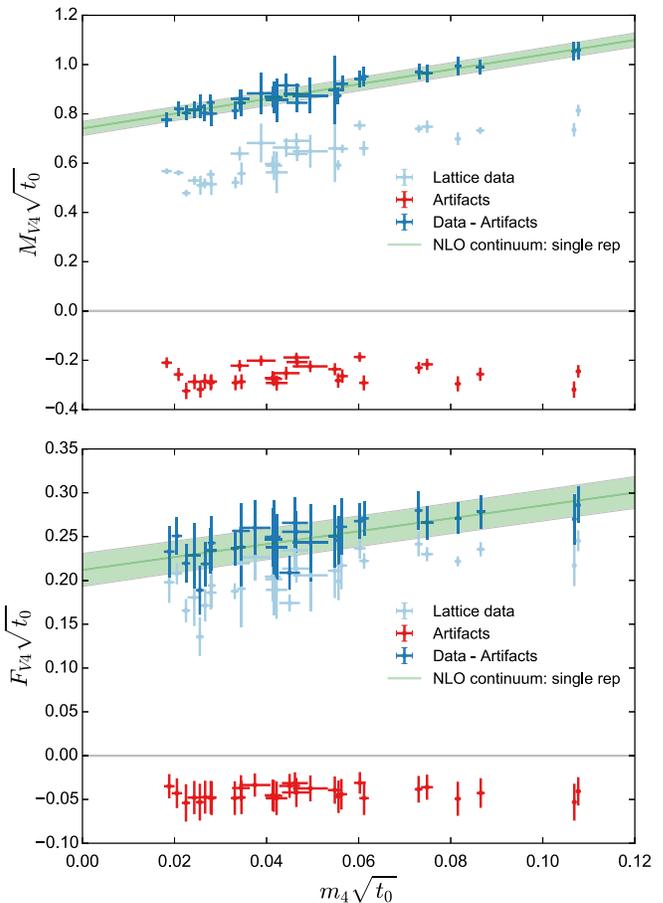
FIG. 12. Breakdown of the contribution of lattice artifacts in the empirical models for the vector masses and decay constants in the fundamental representation.

$$F_V = \sqrt{2}F_P, \qquad (5.3)$$

independent of representation. Figure 14 shows the ratio F_{Vr}/F_{Pr} in each representation, after subtracting lattice
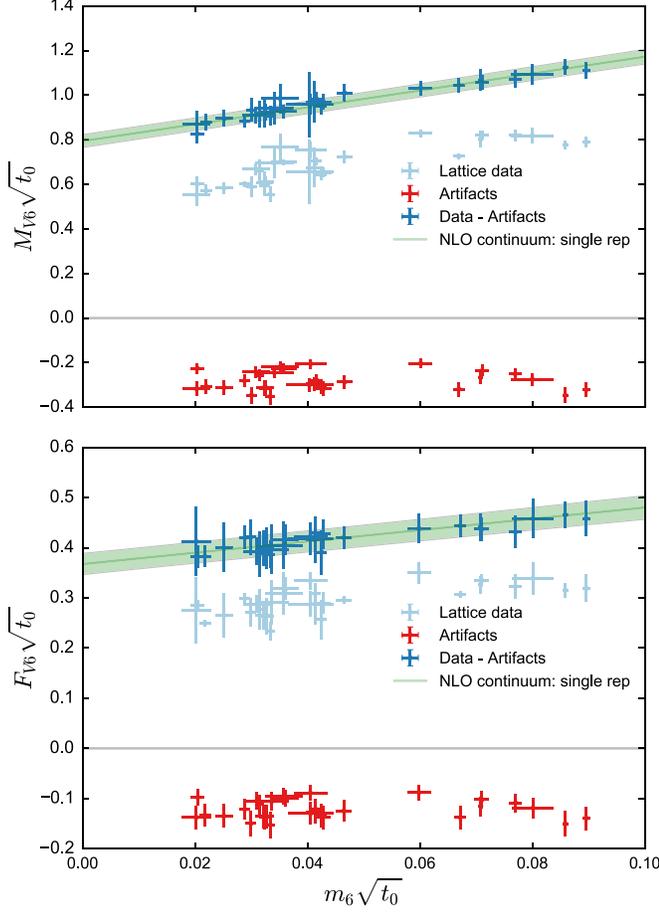
FIG. 13.   Breakdown of the contribution of lattice artifacts in the empirical models for the vector masses and decay constants in the sextet representation.
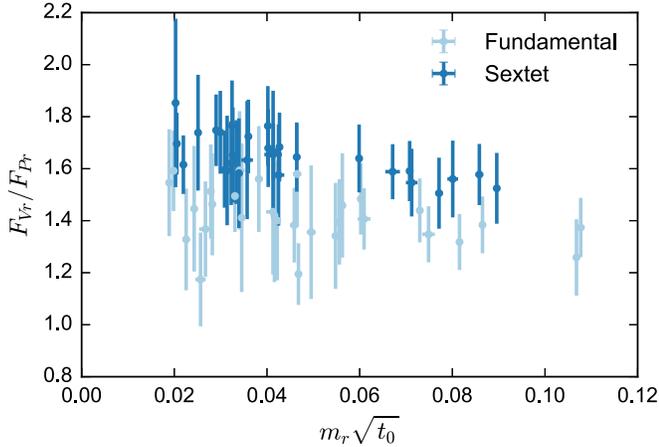
FIG. 14.   Ratio of the vector and pseudoscalar decay constants in each representation. The KSRF prediction is a constant value of $\sqrt{2}$.

artifacts. The KSRF prediction is qualitatively successful. (In QCD, the experimental value is roughly 1.66.)

Another result of KSRF is that the on-shell coupling constant g_{VPP} mediating the decay of a vector into two pseudoscalars is given by

$$g_{VPP} = \frac{M_V}{F_P}. \qquad (5.4)$$

We plot this ratio in Fig. 15. As already noted, in our ensembles the vector meson is stable. Nevertheless, we may use the KSRF result as a phenomenological estimate for the behavior close to the chiral limit. Using the tree-level formula for the $V \rightarrow PP$ decay width in the limit where $M_{Pr} \ll M_{Vr}$,

$$\Gamma_{V \rightarrow PP} \simeq \frac{g_{VPP}^2 M_V}{48\pi}, \qquad (5.5)$$
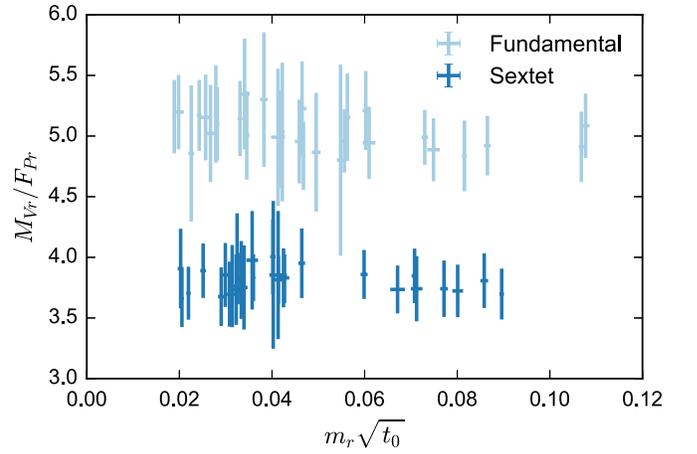
FIG. 15.   Ratio of the vector mass and pseudoscalar decay constant in a fixed representation. KSRF identify this quantity with the coupling g_{VPP}. In QCD, this ratio is roughly 5.9.
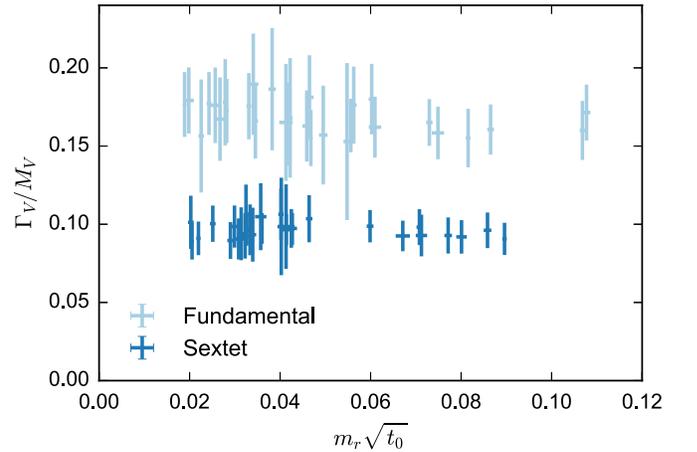
FIG. 16.   Tree-level estimates for the width-to-mass ratio of the vector mesons according to KSRF. The KSRF estimate for this ratio is roughly 0.23 in QCD.

we can estimate the mass-to-width ratio for each vector resonance,

$$\frac{\Gamma_{V\to PP}}{M_V} \simeq \frac{M_V^2}{48\pi F_P^2}. \tag{5.6}$$

From Fig. 15 we thus obtain Fig. 16. For the physical ρ meson, this ratio has a value of roughly 0.23. (The experimental value is 0.19.)

VI. DISCUSSION

A. Large-N_c counting

We want to put our results in context with comparisons to QCD. Large-N_c counting (for N_c colors) is a way to do that. Any quantity Q is expected to scale across N_c as

$$Q(N_c) = N_c^p\left(Q_0 + \frac{Q_1}{N_c} + \frac{Q_2}{N_c^2} + \cdots\right), \tag{6.1}$$

where p is some characteristic exponent determined by large-N_c considerations, and the Q_i are a set of expansion coefficients. Before we get to the (limited) comparisons between different N_c's we can make, our theory gives us a unique opportunity to compare the expansion coefficients for different representations. More specifically, if we neglect all the subleading corrections, our data allow us to compare the leading expansion coefficient Q_0 between the fundamental and two-index antisymmetric representations, for various obesrvables.

We start with meson masses, which are predicted to be independent of N_c [$p = 0$ in Eq. (6.1)]. Figures 3 and 9 reveal near independence of representation of the pseudoscalar and vector masses when plotted against the corresponding fermion mass. This is further supported by the near equality of $\mathring{B}_4$ and $\mathring{B}_6$ in Table I. We conclude that Q_0 is roughly independent of representation for the pseudoscalar and vector meson masses.

Decay constants scale as $\sqrt{N_c}$ for single-index fermions and as N_c for two-index fermions. As for the leading expansion coefficient, a possible guess might be that the product $N_c^p Q_0$ follows the leading large-N_c behavior of $(\dim r)^{1/2}$. This would imply that there exists a constant c such that $Q_0 \approx c$ for mesons made of fundamental-representation fermions, while $Q_0 \approx c/\sqrt{2}$ for mesons made out of fermions in the two-index antisymmetric representation. For $N_c = 4$ we thus expect $F_6/F_4 \approx \sqrt{N_c/2} = \sqrt{2}$. The ratio F_6/F_4 is plotted in Fig. 17 for the pseudoscalar and vector mesons, showing good (perhaps too good) agreement with this expectation. Another consequence is that the ratio F_{Vr}/F_{Pr} is expected to be roughly independent of representation r, in agreement with Fig. 14 and the KSRF relation.
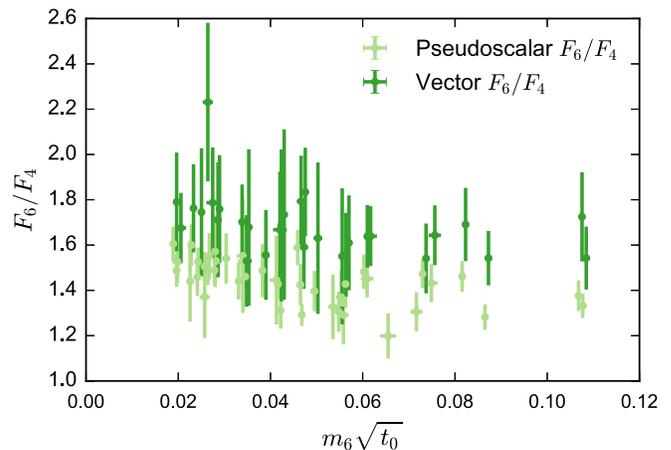
FIG. 17. The ratio of the decay constants in the sextet and fundamental representations in both the pseudoscalar (dark green) and vector (light green) channels.

In this context, we can also compare the fermion condensates in the two representations. We can use the results of the chiral fit to calculate these (per flavor), each in its corresponding chiral limit. Using Eq. (3.19) we find $\hat{\Sigma}_6/\hat{\Sigma}_4 = 2.4(3)$ for the ratio of condensates in the (double) chiral limit, reflecting our empirical findings that $\mathring{B}_6/\mathring{B}_4 \simeq 1$ and $\mathring{F}_6/\mathring{F}_4 \simeq \sqrt{2}$.

Finally, we compare our results for the ratio M_{Vr}/F_{Pr} to the SU(3) case. We expect that this ratio for either SU(4) representation will be smaller than its value in QCD, which is 770 MeV/130 MeV = 5.9. This is borne out by Fig. 15. At a more quantitative level, large-N_c scaling predicts this value to be $5.9 \times \sqrt{3/4} \approx 5.1$ for the fundamental representation, in good agreement with the data. If we regard the fundamental representation of SU(3) as the two-index antisymmetric one, we obtain a large-N_c prediction of $5.9 \times 3/4 \approx 4.4$ for the sextet. While the average value of this ratio is smaller for the sextet, one can say that this prediction is consistent with the general trend of our data. If we add to this the KSRF relation, we find correspondingly smaller values for the width to mass ratio of our vector mesons compared to the physical ρ meson.

B. Conclusions

In this paper we have described the low-lying mesonic spectrum of SU(4) gauge theory coupled to dynamical fermions in the fundamental and sextet representations. These multirep simulations are the first of their kind. Our choice of this theory was inspired by its close similarity to a composite-Higgs model first studied by Ferretti [7].

Our analysis focused on the masses of the pseudoscalar and vector states and their associated decay constants. Using the extension of χPT that accounts for the discretization errors of Wilson fermions, we carried out a global fit of the pseudoscalar masses and decay constants of the

two representations, to NLO in the GSM power-counting scheme. We found significant lattice artifacts, which we were able to subtract, obtaining predictions for continuum-limit values. Our chiral fit provides mild evidence for coupling between the two fermion representations, a novel feature of multirep theories.

Through both the mass terms and the Wilson terms, our lattice setup incorporates the expected symmetry breaking patterns: $SU(2)_L \times SU(2)_R \to SU(2)_V$ in the fundamental sector, and $SU(4) \to SO(4)$ in the sextet sector. We did not carry out a dedicated study of alternative symmetry breaking patterns. Still, the success of the chiral fits provides some confirmation that the above symmetry breaking patterns are the right ones.

The main theoretical uncertainty of our chiral fits concerns the size of N^{2}LO effects. Thanks to a large decay constant, the chiral expansion converges quickly in the sextet sector, supporting the hypothesis that N^{2}LO effects are small in this sector. In the fundamental sector the chiral expansion converges more slowly. Hence, keeping N^{2}LO effects below a certain comfortable level might require the exclusion of ensembles where $\hat{m}_4$ is on the high side. More quantitative statements cannot be made given our data.

The correlation functions that we calculated probe directly the pseudoscalar states made purely of fundamental or purely of sextet fermions. This is reflected in the stability of the LO parameters $\mathring{F}_r$ and $\mathring{B}_r$ if we constrain the maximal value of $\hat{m}_4$ to successively smaller values. The last LO parameter, the decay constant $\mathring{F}_\zeta$ of the axionlike singlet NG boson, is not well determined because we have not calculated propagators in the ζ channel. The ζ meson does contribute through virtual loops to the correlation functions we have studied. Accordingly, our fits depend on $\mathring{F}_\zeta$, but only through NLO logarithmic terms. $\mathring{F}_\zeta$ is more sensitive to the upper limit on $\hat{m}_4$; as a result, so is our prediction for the mass of the ζ boson. Nonetheless, we have argued that the ζ is lighter than the fundamental-sector NG bosons, $M_\zeta < M_4$, in the sextet-chiral limit $\hat{m}_6 \to 0$, a limit which is interesting for the phenomenology of Ferretti's model. In a full composite-Higgs model, however, the masses of all pseudoscalar states can receive important corrections from the couplings to Standard Model fields.

In modeling our results for the vector mesons, we found that the ratio of pseudoscalar to vector decay constants agrees well with the KSRF result based on vector meson dominance. As discussed in Sec. VI A, comparing the KSRF prediction for the decay rate of the vector meson in the chiral limit to the QCD case shows reasonable agreement with large-N_c counting.

Although our estimates for Γ_V/M_V depend on the well-motivated but nonrigorous assumption of vector meson dominance, the resulting narrowness is almost certainly generic. In large-N_c, the widths of mesons made of fundamental-representation fermions scales as $1/\sqrt{N_c}$

and thus they become narrower as N_c increases. Insofar as large-N_c provides the cleanest explanation for the narrowness and existence of mesons in QCD, the vector mesons should become narrower in theories with more colors. We proposed that in multirep theories, the generalization of $\sqrt{N_c}$ is $(\dim r)^{1/2}$, a hypothesis supported by our data. This result is good news for phenomenologists looking to constrain models like the Ferretti model, since narrower states typically provide clearer signals in collider data.

As we have mentioned, we are also exploring the phase diagram of this multirep theory [21]. We have been looking for—and not finding—scale separation between the representations in the confinement and chiral transitions. We are also studying the baryon spectrum, a particularly interesting sector of the theory given its connection to top-quark physics and partial compositeness in the Ferretti model.

Other interesting avenues for the future work in this model (or multirep composite Higgs theories more generally) include quantities related to the Higgs potential. The contribution of the Standard Model's gauge fields to the Higgs potential, Π_{LR}, is conceptually identical to the physics of electromagnetic splittings between pions in QCD and has been the subject of a recent pilot study on the lattice [42]. The top-quark contribution to the Higgs potential is considerably more challenging [43,44].

ACKNOWLEDGMENTS

APPENDIX A: DATA TABLES

In this appendix we show Tables II–XIII.

TABLE II. List of ensembles with $V = 16^3 \times 18$ generated for this study. Configurations are separated by 4 Monte Carlo trajectories.

Ensemble	β	κ_4	κ_6	Configurations
1	7.2	0.13173	0.13423	67
2	7.2	0.1318	0.1341	29
3	7.2	0.132	0.134	42
4	7.3	0.1314	0.1333	17
5	7.3	0.1315	0.1333	17
6	7.308	0.1304	0.1339	29
7	7.31	0.1305	0.1339	17
8	7.32	0.13	0.134	17
9	7.33	0.1314	0.1332	17
10	7.33	0.1314	0.1333	17
11	7.33	0.1315	0.1335	17
12	7.4	0.1307	0.133	17
13	7.4	0.131	0.133	29
14	7.5	0.13	0.132	17
15	7.5	0.13	0.1325	29
16	7.5	0.13	0.1327	29
17	7.5	0.13	0.1328	29
18	7.5	0.1305	0.1327	29
19	7.75	0.129	0.131	29
20	7.75	0.129	0.1315	29

TABLE III. List of ensembles with $V = 16^3 \times 32$. Configurations are separated by 10 Monte Carlo trajectories.

Ensemble	β	κ_4	κ_6	Configurations
21	7.25	0.13095	0.13418	61
22	7.25	0.13147	0.13395	71
23	7.276	0.13157	0.13364	96
24	7.3	0.13117	0.13363	61
25	7.3	0.13118	0.13361	96
26	7.3	0.13162	0.1334	71
27	7.308	0.1304	0.13393	96
28	7.33	0.1314	0.1332	96
29	7.4	0.1307	0.133	96
30	7.55	0.129	0.1325	84
31	7.55	0.13	0.1325	84
32	7.65	0.128	0.131	49
33	7.65	0.129	0.1308	49
34	7.65	0.13	0.131	84
35	7.65	0.13	0.132	84
36	7.75	0.128	0.131	84
37	7.75	0.129	0.1308	54
38	7.75	0.1295	0.1315	34
39	7.85	0.129	0.1308	44

TABLE IV. List of ensembles with $V = 24^3 \times 48$. Configurations are separated by 10 Monte Carlo trajectories.

Ensemble	β	κ_4	κ_6	Configurations
40	7.51	0.1307	0.1328	133
41	7.55	0.13	0.1327	80
42	7.55	0.1305	0.1325	91
43	7.55	0.1307	0.13234	80

TABLE V. Measured gradient flow scale t_0 and fermion masses $\hat{m}_r = m_r \sqrt{t_0}$ in the ensembles with volume $V = 16^3 \times 18$.

Ensemble	t_0/a^2	$\hat{m}_4$	$\hat{m}_6$
1	1.07(2)	0.024(1)	0.022(1)
2	0.92(3)	0.026(2)	0.030(2)
3	0.89(2)	0.023(1)	0.033(1)
4	0.99(3)	0.034(3)	0.043(4)
5	0.93(2)	0.028(2)	0.043(2)
6	1.07(3)	0.056(2)	0.024(2)
7	1.26(2)	0.054(3)	0.023(3)
8	1.20(3)	0.066(4)	0.018(2)
9	1.15(3)	0.027(3)	0.043(3)
10	1.22(1)	0.026(2)	0.037(1)
11	1.40(2)	0.020(1)	0.029(1)
12	1.26(2)	0.041(2)	0.041(4)
13	1.45(2)	0.030(2)	0.039(2)
14	1.09(3)	0.061(3)	0.067(4)
15	1.33(2)	0.056(2)	0.046(2)
16	1.49(4)	0.055(3)	0.035(3)
17	1.67(2)	0.055(2)	0.031(1)
18	1.89(3)	0.034(3)	0.031(3)
19	1.99(6)	0.075(2)	0.071(2)
20	2.38(6)	0.072(3)	0.043(2)

TABLE VI. Same as Table V, but in the ensembles with volume $V = 16^3 \times 32$.

Ensemble	t_0/a^2	$\hat{m}_4$	$\hat{m}_6$
21	1.093(9)	0.042 2(7)	0.020 3(10)
22	1.135(9)	0.027 9(11)	0.025 1(12)
23	1.128(24)	0.024 3(7)	0.032 6(7)
24	1.132(12)	0.034 5(8)	0.032 3(14)
25	1.100(10)	0.033 1(5)	0.032 5(5)
26	1.111(9)	0.022 8(6)	0.0381(8)
27	1.174(10)	0.055 6(7)	0.022 0(9)
28	1.095(12)	0.028 2(7)	0.042 7(7)
29	1.226(10)	0.041 6(8)	0.040 3(8)
30	1.418(12)	0.086 5(11)	0.041 4(15)
31	1.845(18)	0.049 5(11)	0.034 0(13)
32	0.916(5)	0.106 8(8)	0.085 8(15)
33	1.067(5)	0.081 6(10)	0.089 6(8)
34	1.463(15)	0.045 9(18)	0.080 1(22)
35	2.294(22)	0.038 2(13)	0.035 7(21)
36	1.556(12)	0.107 7(12)	0.070 8(10)
37	1.754(15)	0.073 0(19)	0.077 1(16)
38	2.621(20)	0.046 5(13)	0.040 2(14)
39	2.670(22)	0.060 2(14)	0.059 9(12)

TABLE VII. Same as Table V, but in the ensembles with volume $V = 24^3 \times 48$.

Ensemble	t_0/a^2	$\hat{m}_4$	$\hat{m}_6$
40	2.260(16)	0.019 6(4)	0.019 4(9)
41	2.166(11)	0.046 8(5)	0.020 5(4)
42	2.182(12)	0.026 4(5)	0.029 3(6)
43	2.118(6)	0.018 9(5)	0.036 0(7)

TABLE VIII. Measured pseudoscalar masses $\hat{M}_{Pr} = M_{Pr}\sqrt{t_0}$ and decay constants $\hat{F}_{Pr} = F_{Pr}\sqrt{t_0}$ in the ensembles with volume $V = 16^3 \times 18$.

Ensemble	$\hat{M}_{P4}$	$\hat{M}_{P6}$	$\hat{F}_{P4}$	$\hat{F}_{P6}$
1	0.28(1)	0.29(1)	0.102(8)	0.143(8)
2	0.28(2)	0.32(2)	0.106(4)	0.155(6)
3	0.26(1)	0.33(1)	0.109(17)	0.149(15)
4	0.34(3)	0.41(2)	0.115(17)	0.178(33)
5	0.29(2)	0.38(2)	0.108(13)	0.170(11)
6	0.42(2)	0.31(2)	0.120(8)	0.141(19)
7	0.43(2)	0.30(2)	0.132(10)	0.163(23)
8	0.47(1)	0.28(3)	0.138(10)	0.148(19)
9	0.28(2)	0.39(2)	0.110(10)	0.169(10)
10	0.29(2)	0.38(2)	0.129(17)	0.166(28)
11	0.32(5)	0.32(2)	0.113(5)	0.170(11)
12	0.38(2)	0.40(2)	0.127(17)	0.177(23)
13	0.33(1)	0.39(1)	0.115(9)	0.176(11)
14	0.46(2)	0.50(2)	0.142(7)	0.199(9)
15	0.45(1)	0.43(1)	0.133(10)	0.183(14)
16	0.45(2)	0.38(2)	0.141(14)	0.184(19)
17	0.46(1)	0.36(1)	0.145(9)	0.179(14)
18	0.35(2)	0.35(2)	0.122(11)	0.185(13)
19	0.53(2)	0.55(2)	0.159(6)	0.223(17)
20	0.53(2)	0.43(3)	0.153(14)	0.190(20)

TABLE IX. Same as Table VIII, but in the ensembles with volume $V = 16^3 \times 32$.

Ensemble	$\hat{M}_{P4}$	$\hat{M}_{P6}$	$\hat{F}_{P4}$	$\hat{F}_{P6}$
21	0.366(9)	0.263(10)	0.119(6)	0.142(9)
22	0.305(9)	0.303(8)	0.105(4)	0.151(5)
23	0.275(6)	0.341(7)	0.108(4)	0.162(5)
24	0.340(5)	0.340(9)	0.119(4)	0.168(9)
25	0.339(3)	0.344(6)	0.107(4)	0.148(13)
26	0.279(7)	0.368(11)	0.103(4)	0.167(13)
27	0.423(4)	0.279(5)	0.127(4)	0.159(7)
28	0.300(8)	0.391(8)	0.115(6)	0.173(6)
29	0.372(6)	0.391(4)	0.126(3)	0.173(8)
30	0.559(8)	0.408(12)	0.156(6)	0.187(7)
31	0.429(10)	0.375(9)	0.140(9)	0.189(10)
32	0.597(8)	0.554(5)	0.159(9)	0.208(13)
33	0.514(8)	0.576(9)	0.154(8)	0.219(11)
34	0.412(9)	0.565(9)	0.141(7)	0.224(8)
35	0.400(9)	0.408(10)	0.132(6)	0.192(17)
36	0.636(7)	0.538(8)	0.166(6)	0.210(8)
37	0.530(5)	0.571(7)	0.154(4)	0.223(12)
38	0.443(14)	0.428(15)	0.135(9)	0.188(13)
39	0.505(13)	0.529(17)	0.148(8)	0.216(8)

TABLE X. Same as Table VIII, but in the ensembles with volume $V = 24^3 \times 48$.

Ensemble	$\hat{M}_{P4}$	$\hat{M}_{P6}$	$\hat{F}_{P4}$	$\hat{F}_{P6}$
40	0.278(4)	0.291(10)	0.114(4)	0.167(7)
41	0.418(5)	0.295(7)	0.139(4)	0.169(4)
42	0.317(6)	0.355(8)	0.125(4)	0.182(8)
43	0.267(9)	0.394(8)	0.114(4)	0.184(5)

TABLE XI. Measured vector masses $\hat{M}_{Vr} = M_{Vr}\sqrt{t_0}$ and decay constants $\hat{F}_{Vr} = F_{Vr}\sqrt{t_0}$ in the ensembles with volume $V = 16^3 \times 18$. Some ensembles did not yield reliable measurements of F_{Vr} because of insufficient statistics. The figures and tables omit data from such ensembles.

Ensemble	$\hat{M}_{V4}$	$\hat{M}_{V6}$	$\hat{F}_{V4}$	$\hat{F}_{V6}$
1	0.50(3)	0.57(4)	⋯	⋯
2	0.51(8)	0.59(6)	0.14(3)	0.27(4)
3	0.48(3)	0.56(9)	0.17(3)	0.23(4)
4	0.56(6)	0.67(5)	⋯	⋯
5	0.54(7)	0.61(4)	⋯	⋯
6	0.62(2)	0.62(6)	⋯	⋯
7	0.61(4)	0.60(8)	⋯	⋯
8	0.62(4)	0.61(16)	⋯	⋯
9	0.52(7)	0.64(7)	0.17(4)	0.26(4)
10	0.56(8)	0.63(5)	⋯	⋯
11	0.56(14)	0.60(5)	0.21(3)	0.30(4)
12	0.60(6)	0.67(14)	0.20(4)	0.29(3)
13	0.60(8)	0.69(4)	⋯	⋯
14	0.66(4)	0.73(4)	0.22(2)	0.31(3)
15	0.66(3)	0.72(4)	0.22(2)	0.30(2)
16	0.66(4)	0.68(9)	⋯	⋯
17	0.66(3)	0.66(3)	0.21(1)	0.28(1)
18	0.64(8)	0.67(5)	0.22(3)	0.29(7)
19	0.75(4)	0.82(3)	0.23(2)	0.34(4)
20	0.74(4)	0.77(10)	⋯	⋯

TABLE XII. Same as Table XI, but in the ensembles with volume $V = 16^3 \times 32$.

Ensemble	$\hat{M}_{V4}$	$\hat{M}_{V6}$	$\hat{F}_{V4}$	$\hat{F}_{V6}$
21	0.56(2)	0.55(3)	0.19(2)	0.275(1)
22	0.51(2)	0.58(3)	0.17(3)	0.265(1)
23	0.53(3)	0.61(1)	0.18(1)	0.263(1)
24	0.56(2)	0.61(2)	0.19(1)	0.265(2)
25	0.52(3)	0.59(2)	0.19(1)	0.265(1)
26	0.50(3)	0.62(2)	⋯	⋯
27	0.59(2)	0.57(3)	0.20(1)	0.250(2)
28	0.55(3)	0.65(2)	0.19(1)	0.290(3)
29	0.59(1)	0.66(2)	0.20(1)	0.287(1)
30	0.73(2)	0.71(2)	0.24(3)	0.308(2)
31	0.65(2)	0.70(5)	0.21(1)	0.291(2)
32	0.74(1)	0.78(1)	0.24(2)	0.316(2)
33	0.70(1)	0.79(1)	0.22(1)	0.319(1)
34	0.66(3)	0.82(3)	0.22(3)	0.339(2)
35	0.68(5)	0.77(5)	0.20(5)	0.310(3)
36	0.81(1)	0.80(3)	0.25(1)	0.326(2)
37	0.74(2)	0.82(2)	0.23(4)	0.322(4)
38	0.69(4)	0.76(5)	0.24(2)	0.334(3)
39	0.75(2)	0.83(2)	0.24(2)	0.350(4)

TABLE XIII. Same as Table XI, but in the ensembles with volume $V = 24^3 \times 48$.

Ensemble	$\hat{M}_{V4}$	$\hat{M}_{V6}$	$\hat{F}_{V4}$	$\hat{F}_{V6}$
40	0.57(6)	0.61(2)	$\cdots$	$\cdots$
41	0.64(2)	0.60(4)	0.17(1)	0.29(2)
42	0.59(3)	0.66(5)	$\cdots$	$\cdots$
43	0.57(3)	0.70(2)	0.20(2)	0.32(1)

APPENDIX B: TECHNICAL MATTERS—LATTICE

1. Correlator fitting

In calculating correlation functions, we use a smeared source operator on the $t = 0$ time slice while using both point and smeared operators at the sink, projected onto zero spatial momentum. Smearing is done after fixing to the Coulomb gauge, always with smearing radius $r_0 = 6a$. On the large lattices we use antiperiodic boundary conditions in time for the fermion propagators. For the $V = 16^3 \times 18$ ensembles, on the other hand, we superimpose propagators computed with periodic and anti-periodic boundary conditions, which effectively doubles the temporal size of the lattice—a technique sometimes called the "P+A trick" (see Ref. [45] and references therein).

After restricting each correlator to a range $[t_{\min}, t_{\max}]$ we find acceptable fits with single-exponential models, that is, without inclusion of excited states. In each representation, we extract the fermion mass m_r from the axial Ward identity (2.3) via joint fits to the $\langle AP \rangle$ and $\langle PP \rangle$ correlators with a point sink.

We use the publicly available Python packages LSQFIT [46] and GVAR [47] for nonlinear fitting and classical error propagation. When computing ratios of quantities derived from different fits, we use single-elimination jackknife to propagate errors including correlations.

For each correlator, our fitting procedure is as follows. First, we vary the initial and final times $[t_{\min}, t_{\max}]$ used in the fits, amounting to a grid search over possible range fits. The best fit is chosen automatically using a criterion from the QCD literature with a preference for small χ^2/dof, large fit ranges, and well-determined fit parameters [48]. We maximize

$$Q \equiv \frac{p \times N_{\mathrm{dof}}}{\sum_n \sigma_{p_n}^2}, \qquad \text{(B1)}$$

where p is the unconstrained p-value, N_{dof} denotes the number of degrees of freedom in the fit, and σ_{p_n} denotes the statistical error in the nth fit parameter. Although this criterion is ultimately arbitrary, it coincides with intuition about which fits ought to be considered good and removes subjective bias. We confirm that masses emerging from this procedure are consistent with expectations from effective mass plots; a representative comparison is shown in Fig. 18. We have also experimented with a "two-state" double-exponential ansatz,
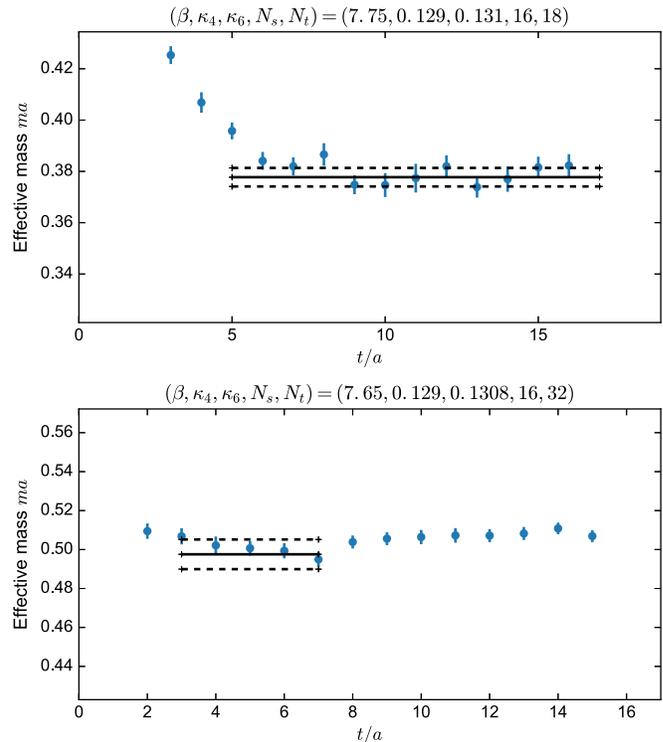
FIG. 18. Representative plot showing the effective mass ma extracted from a smeared-source, point-sink pseudoscalar correlator on a typical $16^3 \times 18$ ensemble (top) and $16^3 \times 32$ ensemble (bottom) used in this study. The black lines indicate the mass and error (including range-fit systematic uncertainty) extracted from a full nonlinear fit of the correlator. The horizontal width of the black lines indicates the starting and ending times (t_i, t_f) used in the best range fit as determined by the MILC criterion. Note that in the lower panel, the small difference between the central value from the best fit and the effective mass at larger t/a is covered by the statistical + systematic error band, showing that our range-fit uncertainty is working as expected.

observing no significant changes in the ground-state masses within the combined statistical and systematic errors estimated using this procedure.

For an estimate of the systematic uncertainty associated with our fit-choice procedure, we compute the spread in the model parameters emerging from all nominally good fits satisfying $Q \geq 0.1$. We then combine the statistical and systematic uncertainties conservatively using

$$\sigma_{\mathrm{tot}} = \sigma_{\mathrm{stat}} + \sigma_{\mathrm{syst}}. \qquad \text{(B2)}$$

The systematic error assigned by this procedure is often comparable to the statistical error, and is occasionally significantly larger. The error estimates for the fermion masses m_r in Tables V–XIII include this fit-range systematic.

2. Decay constants and operator renormalization

The lattice operators appearing in the correlation functions are subject to finite renormalization in order to obtain

the continuum-normalized operators that are required for determination of decay constants. We carry out this procedure in lattice perturbation theory including tadpole improvement; the procedure is described in Appendix D. The explicit relationship between lattice and continuum operators is given by Eq. (D28).

Simultaneous fits to the smeared-source, point-sink (s, p) and smeared-source, smeared-sink (s, s) correlation functions allow us to extract the mass, decay constant, and smeared amplitude. For example, the $\langle VV \rangle$ correlators in representation r give us the vector decay constant F_{Vr} defined in Eq. (5.1). The fit functions are

$$C_{Vr}^{(s,p)}(t) = \frac{A_{Vr}^s A_{Vr}^p}{2M_{Vr}}(e^{-M_{Vr}t} + e^{-M_{Vr}(T-t)}), \quad \text{(B3)}$$

$$C_{Vr}^{(s,s)}(t) = \frac{A_{Vr}^{s\;2}}{2M_{Vr}}(e^{-M_{Vr}t} + e^{-M_{Vr}(T-t)}), \quad \text{(B4)}$$

giving the vector mass M_{Vr} and the point and smeared amplitudes A_{Vr}^p and A_{Vr}^s, respectively. In order to obtain decay constants with continuum normalizations, we apply the renormalization factors of Eq. (D28). The result is

$$F_{Vr} = Z_{Vr}\left(1 - \frac{3\kappa_r}{4\kappa_r^c}\right)\frac{A_{Vr}^p}{M_{Vr}}. \quad \text{(B5)}$$

3. Fermion mass determination and κ_r^c

To determine the critical values κ_r^c, which enter into the field normalization for decay constants defined in Appendix B 2, we perform a global fit to the AWI fermion masses in units of the flow scale t_0 as given in Tables V–VII. We use the model function

$$\sqrt{t_0}m_4 = c_0 + c_1\beta + \kappa_4(d_0 + d_1\beta) + \kappa_6(d_0' + d_1'\beta) \quad \text{(B6)}$$

and similarly for $\sqrt{t_0}m_6$ (with a separate set of coefficients). We find that these terms, which are a subset of all possible combinations of the bare parameters $\{\beta, \kappa_4, \kappa_6\}$ through quadratic order, are sufficient to provide reasonable fit quality.

Since we are interested in the regions where $m_r \to 0$, we use only those ensembles that have $\sqrt{t_0}m_r < 0.08$, a value determined empirically by inspecting our data for deviations from the simple analytic behavior of Eq. (B6). Our fits give χ^2/dof of 16/24 and 21/24 for fitting $\sqrt{t_0}m_4$ and $\sqrt{t_0}m_6$, respectively. The resulting κ_c curves at two β values are shown in Fig. 19.

As noted above, because κ_c is determined by extrapolation, we do not probe the existence of a possible Aoki phase.

4. Study of finite-volume corrections

All of our ensembles satisfy the criterion $M_{Pr}L > 4$ for both pseudoscalar meson masses. Using Eq. (3.18) with the results of our central fit, we further verify that $M_\zeta L > 4$ in all cases. Although this cut is known to provide a useful threshold for the suppression of finite volume effects in QCD, since we are studying a new system a more cautious treatment is worthwhile. Here we present three different analyses and arguments which lead us to estimate that finite-volume effects are no more than a few percent for our data, and are thus not resolved within the uncertainty of our results. One particular source of finite-volume effects can be the freezing of the evolution of topological charge [49,50]; we measure the topological charge Q on our ensembles using the Wilson flow to smear the gauge fields out to $t/a^2 = 5.0$ and find an acceptable distribution of Q in all cases.
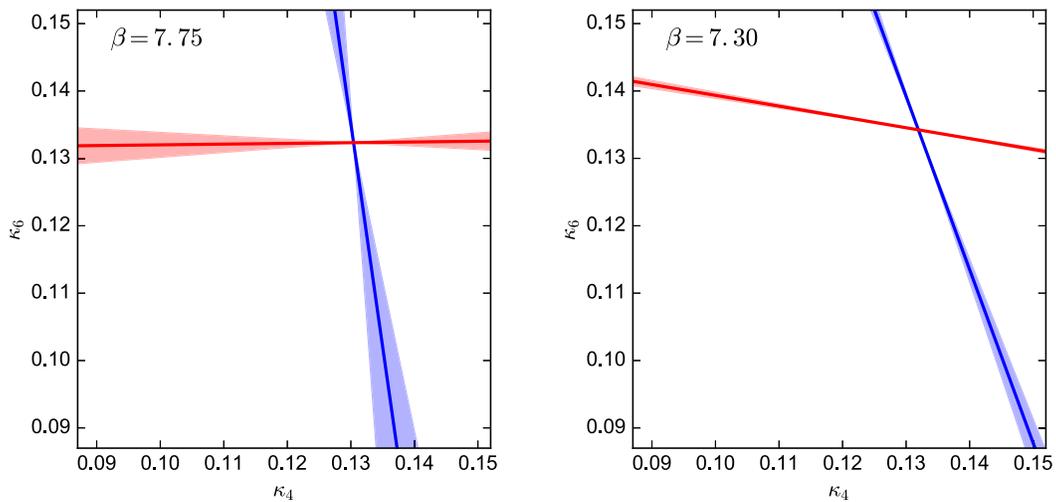
FIG. 19. κ_c curves with uncertainties for both representations at two values of the bare coupling β, based on our fits to $\sqrt{t_0}m_r$ as described in the text. The red (horizontal) curve is where m_6 vanishes, defining the function $\kappa_6^c(\beta, \kappa_4)$. The blue (vertical) curve is where m_4 vanishes, defining $\kappa_4^c(\beta, \kappa_6)$.
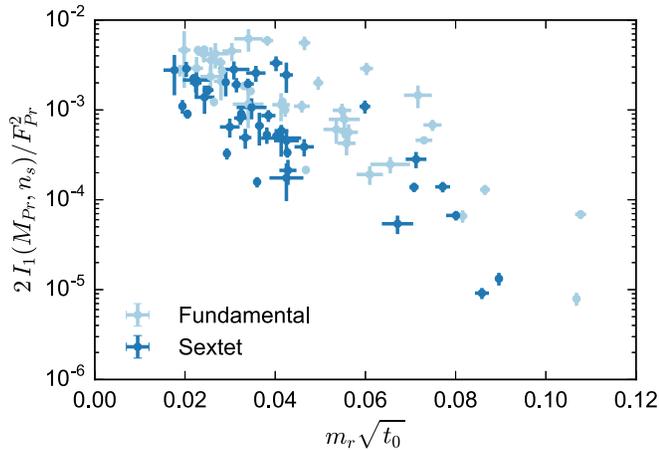
FIG. 20. Quantifying the size of leading-order finite volume corrections, Eq. (B7).

First, to obtain a theoretical estimate of the expected size of finite-volume effects, we consider the size of leading-order finite-volume correction to tadpole diagrams in chiral perturbation theory [9,32,51]. The dimensionless figure of merit for this effect is $2I_1(M_{Pr}, L)/F_{Pr}^2$, where

$$I_1(M, L) = 6\left(\frac{M^2}{16\pi^2}\right)\sqrt{\frac{8\pi}{(ML)^3}}e^{-ML}. \quad (B7)$$

This quantity gauges the effect of mesons interacting with their finite-volume image points. In Fig. 20 we plot

$2I_1(M_{Pr}, L)/F_{Pr}^2$ for all of our ensembles, with each representation r plotted against the corresponding $\hat{m}_r$. We therefore expect that finite volume corrections do not exceed a few percent in the ensembles of this study. This formula assumes the applicability of chiral perturbation theory, which requires that $F_{Pr}L \gtrsim 1$; over all of our ensembles we find that $F_{P4}L \gtrsim 1.3$ and $F_{P6}L \gtrsim 1.9$.

Second, we recalculate the observables M_{Pr}, F_{Pr}, and t_0 on ensembles with several spatial volumes at two sets of bare parameters, $(\beta, \kappa_4, \kappa_6) = (7.75, 0.128, 0.131)$ and $(7.75, 0.129, 0.1308)$. These bare parameters match the production $V = 16^3 \times 32$ ensembles 36 and 37 as listed in Table III. Four ensembles hold $N_t = 32$ fixed and vary the spatial volume as $N_s = 12, 14, 16, 18$; the fifth ensemble at each point has $N_s = 24$ and $N_t = 48$.

Results of this test are shown in Figs. 21–23 below. For both sets of bare parameters, all observables down to the smallest $N_s = 12$ are seen to be within $\pm 5\%$ of the central value obtained on $N_s = 24$, and within 2%–3% for $N_s = 16$ which is the smallest spatial volume used in our central analysis.

Finally, we have included explicit variation of the finite-volume cut on pseudoscalar meson masses (i.e., minimum cut on $M_{P_r}L$) in the stability analysis of our central chiral fit, as presented in Sec. IV B and Fig. 7. We also consider the effects of the finite temporal direction by cutting the $N_t = 18$ ensembles out of the analysis. All of the fit results are seen to be stable at the one-sigma level as we vary the finite-volume cut. We conclude that finite-volume effects are not significant in our results at the level of precision we obtain.
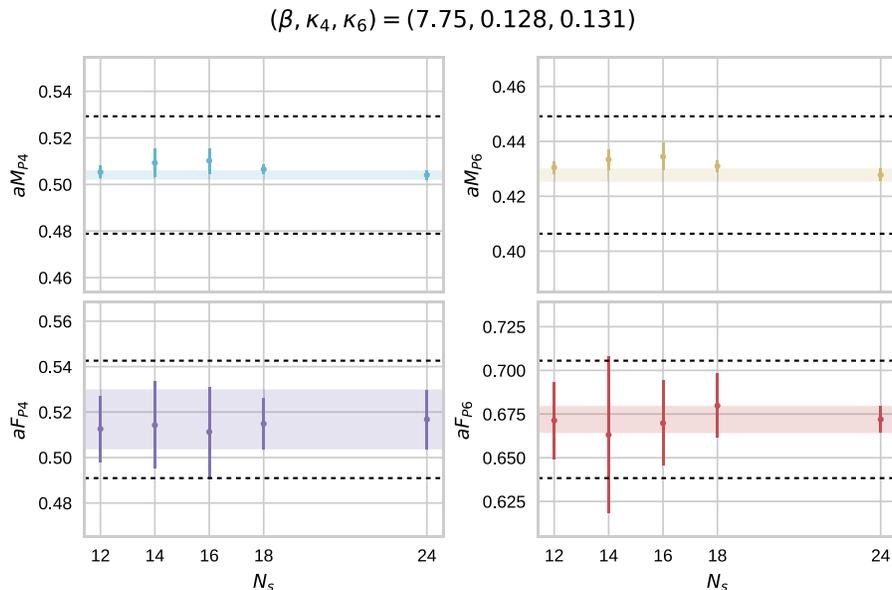
$$(\beta, \kappa_4, \kappa_6) = (7.75, 0.128, 0.131)$$

FIG. 21. Explicit test of the dependence of the pseudoscalar masses and decay constants on spatial volume at bare parameters $(\beta, \kappa_4, \kappa_6) = (7.75, 0.128, 0.131)$. The dashed lines indicate variations of $\pm 5\%$ with respect to the mean value of the rightmost $N_s = 24$ point.
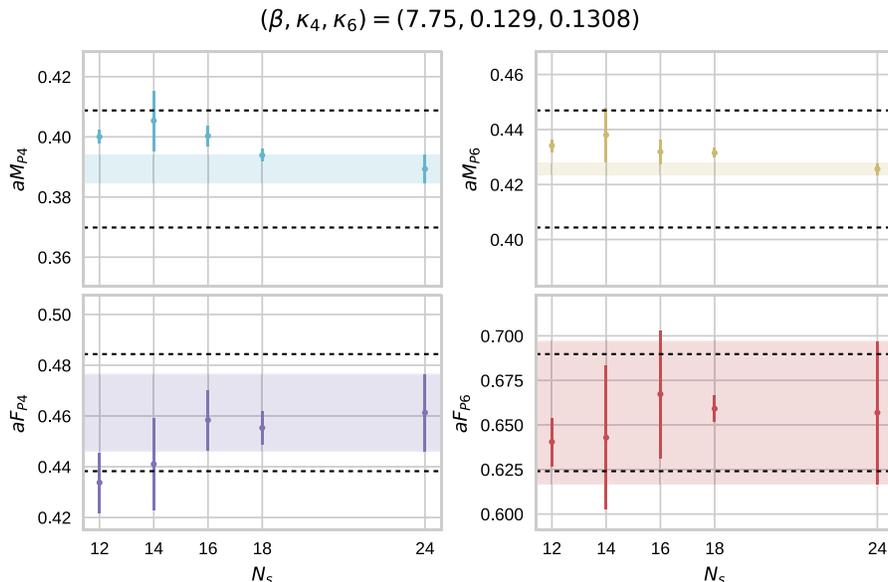
$(\beta, \kappa_4, \kappa_6) = (7.75, 0.129, 0.1308)$

FIG. 22. Explicit test of the dependence of the pseudoscalar masses and decay constants on spatial volume at bare parameters $(\beta, \kappa_4, \kappa_6) = (7.75, 0.129, 0.1308)$. The dashed lines indicate variations of $\pm 5\%$ with respect to the mean value of the rightmost $N_s = 24$ point.
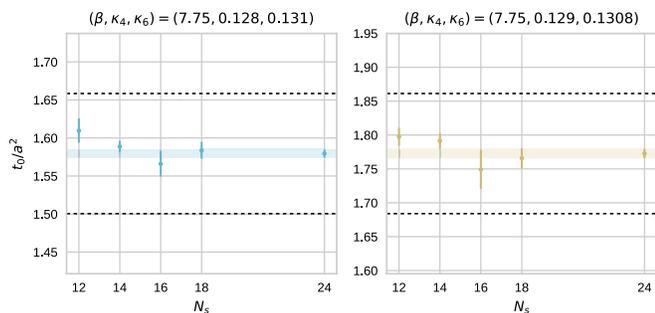
FIG. 23. Explicit test of the dependence of the Wilson flow scale t_0/a^2 on spatial volume at two sets of bare parameters, as described in the text. The dashed lines indicate variations of $\pm 5\%$ with respect to the mean value of the rightmost $N_s = 24$ point.

APPENDIX C: TECHNICAL MATTERS—THE AXIAL CURRENT AND WχPT

1. Conserved U(1) axial current

The conserved axial current is given by

$$J_{5\mu} = \sum_{r=4,6} q_r J_{5\mu}^{(r)}. \tag{C1}$$

As usual, the normalization of U(1) currents is arbitrary. We normalize the individual axial currents $J_{5\mu}^{(r)}$ such that all right-handed fields have unit charge. The ratio q_4/q_6 is then fixed by the group traces of the two representations. For the normalization of $J_{5\mu}$ we adopt the same prescription as in Ref. [12]. The resulting charges are

$$q_4 = \frac{2}{\sqrt{5}}, \qquad q_6 = -\frac{1}{\sqrt{5}}. \tag{C2}$$

These charges were used in the χPT formulas of Sec. III C.

Tracing Eqs. (3.13)–(3.16) back to the general NLO expressions of Ref. [12], one can check that they only depend on the ratios q_r/F_ζ. These ratios are independent of the choice of normalization for the axial current, because a rescaling of $J_{5\mu}$ by a factor λ implies a rescaling by the same factor of both the charges q_4 and q_6 and of the singlet's decay constant F_ζ. All other LECs in Eqs. (3.13)–(3.16) are independent of this rescaling (for more details, see Ref. [12]). Of course, once the normalization of the charges is fixed according to Eq. (C2), the normalization of F_ζ is fixed as well.

2. AWI mass and Wilson chiral perturbation theory

In this appendix we review the proof of Ref. [35] that the mass defined by imposing the axial Ward identity, m_{AWI}, is equal to the shifted mass m_{shifted}, which is the mass parameter occurring in the LO Lagrangian of WχPT, up to higher-order corrections. For simplicity, we will consider the GSM power counting used throughout this paper.

A nice feature of the GSM scheme is that the LO lagrangian takes the same form as in the continuum. The reason is that the only new operator at $O(a)$ is the Pauli term $a\bar{\psi}\sigma_{\mu\nu}F_{\mu\nu}\psi$, which has the same chiral transformation properties as the fermion mass term. The Pauli term enters the Symanzik action with a coefficient that depends linearly on the parameter c_{SW} of the clover term in the Wilson action. After the transition to the chiral effective theory, the nonderivative terms in the LO Lagrangian take the form

$$\mathcal{L}_m = -\frac{F^2}{4}\text{tr}(\chi^\dagger\Sigma + \Sigma^\dagger\chi) - \frac{F^2}{4}\text{tr}(\hat{A}^\dagger\Sigma + \Sigma^\dagger\hat{A}), \quad \text{(C3)}$$

where the mass term has been mapped to the first term on the right-hand side, and the Pauli term to the second. χ is the usual spurion of continuum χPT, and $\hat{A}$ is a new spurion with the same chiral transformation properties as χ. The "expectation values" of the spurions are [52]

$$\chi = 2Bm_{\text{ctm}}, \qquad \hat{A} = 2W_0 a, \quad \text{(C4)}$$

where B and W_0 are low-energy constants. Substituting back into Eq. (C3) gives

$$\begin{aligned}\mathcal{L}_m &= -\frac{F^2}{4}(2Bm_{\text{ctm}} + 2W_0 a)\text{tr}(\Sigma + \Sigma^\dagger) \\ &= -\frac{F^2}{2}Bm_{\text{shifted}}\text{tr}(\Sigma + \Sigma^\dagger), \quad \text{(C5)}\end{aligned}$$

where the shifted mass is defined by Eq. (3.10). For brevity, in the rest of this appendix we denote the shifted mass as m.

As explained in Sec. II B, in our numerical simulations we define the fermion mass m_{AWI} by imposing the axial Ward identity, Eq. (2.3). Before we can use WχPT, we need to know the relation between m_{AWI} and the shifted mass m of Eq. (3.10), in terms of which the chiral expansion is done.

This relation was analyzed carefully in Ref. [35] for the case of two-flavor QCD. The pseudoscalar density that was considered there, and which is also used in our work, is the usual local density,[3]

$$P^a_{\text{loc}} = \bar{\psi}\gamma_5 T^a\psi. \quad \text{(C6)}$$

For the axial current, Ref. [35] considered

$$A^a_\mu = A^a_{\mu,\text{loc}} + ac_A\partial_\mu P^a_{\text{loc}}, \quad \text{(C7)}$$

where ∂_μ stands for a lattice derivative; the local axial current is

$$A^a_{\mu,\text{loc}} = \bar{\psi}\gamma_5\gamma_\mu T^a\psi. \quad \text{(C8)}$$

For the purpose of this discussion, we may consider c_A in Eq. (C7) as a free parameter. In our numerical simulations we use the naive axial current, which corresponds to $c_A = 0$.

To first order in the pion field, the lattice operators are mapped to the effective theory according to

$$P^a_{\text{eff}} = \sqrt{2}FB\pi^a(1 + O(a)), \quad \text{(C9)}$$

$$A^a_{\mu,\text{eff}} = \sqrt{2}F\partial_\mu\pi^a(1 + O(a)), \quad \text{(C10)}$$

---

[3]In this subsection we disregard renormalization factors.

where π^a is the effective pion field. The precise form of the $O(a)$ corrections may be found in Ref. [35]. In both equations, they depend linearly on the clover parameter c_{SW}. In addition, the $O(a)$ correction in Eq. (C10) depends linearly on c_A. Plugging this into Eq. (2.3) and using the LO pion mass, given by $M^2 = 2Bm$, we find

$$m_{\text{AWI}} = m(1 + O(a)) + O(a^2). \quad \text{(C11)}$$

To the order we are working, in general one expects also an $O(m^2)$ correction. This correction vanishes, however, because the continuum theory satisfies $m_{\text{AWI}} = m$ identically. While the derivation of Ref. [35] was given for a complex representation, a similar argument applies to real (or pseudoreal) representations.

Equation (C11) is robust in that changing the clover coefficient c_{SW} or changing the parameter c_A in Eq. (C7) will change the $O(am)$ corrections, but will not affect the simultaneous vanishing of m_{AWI} and the shifted mass m. This feature is disrupted only by $O(a^2)$ effects, which is as it should be. Indeed, as shown in Ref. [27], depending on the sign of a particular $O(a^2)$ LEC, in the region where $m \sim a^2$ one either encounters the Aoki phase, or a first-order discontinuity line at which the pion mass reaches a nonzero minimum.

As a corollary of Eq. (C11), we may use the value of m_{AWI}, taken from the numerical simulations, for the shifted mass m. At the order we are working, the differences between the two are absorbed into a redefinition of NLO parameters of the chiral expansion.

APPENDIX D: GLUON PROPAGATOR AND PERTURBATIVE CALCULATIONS FOR nHYP LINKS

To perform one loop perturbation theory for the NDS action [20], we need the gluon propagator. This appendix describes its construction and gives perturbative results for current renormalization factors.

Normalized hypercubic links $V_{x,\mu}$ are constructed from the dynamical gauge field $U_{x,\mu}$ via three successive smearing steps [16,17]. Each step uses a weighted sum over staples, which is then reunitarized. Explicitly,

$$\begin{aligned}\Omega_{x,\rho;\xi} &= (1 - \alpha_3)U_{x,\rho} + \frac{\alpha_3}{2}(U_{x,\xi}U_{x+\hat{\xi},\rho}U^\dagger_{x+\hat{\rho},\xi} \\ &\quad + U^\dagger_{x-\hat{\xi},\xi}U_{x-\hat{\xi},\rho}U_{x-\hat{\xi}+\hat{\rho},\xi}), \\ \bar{V}_{x,\rho;\xi} &= \mathcal{P}(\Omega_{\xi,\rho;\xi}), \quad \text{(D1a)}\end{aligned}$$

$$\begin{aligned}\bar{\Omega}_{x,\mu;\nu} &= (1 - \alpha_2)U_{x,\mu} + \frac{\alpha_2}{4}\sum_{\substack{\rho\neq\mu,\nu \\ \xi\neq\mu,\nu,\rho}}(\bar{V}_{x,\rho;\xi}\bar{V}_{x+\hat{\rho},\mu;\xi}\bar{V}^\dagger_{x+\hat{\mu},\rho;\xi} \\ &\quad + \bar{V}^\dagger_{x-\hat{\rho},\rho;\xi}\bar{V}_{x-\hat{\rho},\mu;\xi}\bar{V}_{x-\hat{\rho}+\hat{\mu},\rho;\xi}), \\ \tilde{V}_{x,\mu;\nu} &= \mathcal{P}(\bar{\Omega}_{x,\mu;\nu}), \quad \text{(D1b)}\end{aligned}$$

$$\tilde{\Omega}_{x,\mu} = (1 - \alpha_1)U_{x,\mu} + \frac{\alpha_1}{6}\sum_{\nu\neq\mu}(\tilde{V}_{x,\nu;\mu}\tilde{V}_{x+\hat{\nu},\mu;\nu}\tilde{V}^\dagger_{x+\hat{\mu},\nu;\mu}$$

$$+ \tilde{V}^\dagger_{x-\hat{\nu},\nu;\mu}\tilde{V}_{x-\hat{\nu},\mu;\nu}\tilde{V}_{x-\hat{\nu}+\hat{\mu},\nu;\mu}),$$

$$V_{x,\mu} = \mathcal{P}(\tilde{\Omega}_{x,\mu}). \tag{D1c}$$

The reunitarization operator $\mathcal{P}$ is defined as

$$V = \mathcal{P}(\Omega) \equiv \Omega Q^{-1/2}, \tag{D2}$$

where

$$Q = \Omega^\dagger\Omega. \tag{D3}$$

The best way to understand the smearing is to go in reverse order. The staple sum extends into a different direction at each smearing step, such that each fat link $V_{x,\mu}$ depends on a particular thin link $U_{y,\nu}$, if and only if there exists a hypercube to which both $V_{x,\mu}$ and $U_{y,\nu}$ belong.

The dislocation-suppressing action adds a new term to the pure-gauge action S_g

$$S_g = S_{\text{plaq}} + S_{\text{NDS}}, \tag{D4}$$

where the new term is

$$S_{\text{NDS}} = \frac{1}{2N_c}\sum_x\text{tr}\left(\gamma_1\sum_\mu\tilde{Q}^{-1}_{x,\mu} + \gamma_2\sum_{\mu\neq\nu}\bar{Q}^{-1}_{x,\mu;\nu} + \gamma_3\sum_{\rho\neq\xi}Q^{-1}_{x,\rho;\xi}\right). \tag{D5}$$

In practice we fix the α_i's and take $\gamma_1 = \gamma_2 = \gamma_3 = \gamma = z\beta$ where z is held constant. The weak-coupling expansion to be sketched below gives the bare coupling g_0^2 as

$$\frac{1}{g_0^2} = \frac{\beta}{2N_c} + \frac{1}{N_c}\left(\frac{\gamma_1\alpha_1}{3} + \gamma_2\alpha_2 + \gamma_3\alpha_3\right). \tag{D6}$$

To construct the gluon propagator we need to compute the gauge action in quadratic order. This is pretty standard; a good reference is Ref. [53]. We take the lattice action,

$$S = a^4\sum_x\mathcal{L}(\bar{\psi}, \psi, U), \tag{D7}$$

and replace the link field by an expansion in terms of gauge fields

$$U_\mu(x) = \exp[igaA_\mu(x)]$$

$$= 1 + igaA_\mu(x) - \frac{1}{2}g^2a^2A_\mu(x)^2 + \cdots, \tag{D8}$$

where $A_\mu(x) = \sum_a(\lambda^a/2)A^a_\mu$ gives the decomposition into color components. There is an identical expansion for the fat link, which we write as $V_\mu(x) = \exp[igaB_\mu(x)]$.

The action has an expansion in powers of A. In terms of the integral over the four-dimensional Brillouin zone,

$$\int_q \equiv \int_{-\pi/a}^{\pi/a}\frac{d^4q}{(2\pi)^4}, \tag{D9}$$

and the vector potential,

$$A_\mu(x) = \int_q A_\mu(q)e^{iq(x+a\hat{\mu}/2)}, \tag{D10}$$

the free gauge boson action is

$$S_0^G = -\frac{1}{2}\int_{pp'}(2\pi)^4\delta^4(p+p')[A^a_\mu(p')D^{ab}_{\mu\nu}(p)A^b_\nu(p)]. \tag{D11}$$

For the gauge boson, $D^{ab}_{\mu\nu} = \delta^{ab}D_{\mu\nu}$. Just as in a continuum theory, the gauge boson action cannot be inverted to give the propagator without fixing the gauge. A conventional choice for a gauge fixing term is [introducing $\hat{k}^\mu = 2/a\sin(ak_\mu/2)$]

$$S_{\text{gf}} = -\frac{1}{2}\sum_{\mu\nu}\int_k\text{Tr}\frac{1}{\xi}\hat{k}_\mu\hat{k}_\nu A^a_\mu(-k)A^a_\nu(k). \tag{D12}$$

Then the gauge boson propagator is found by solving the field equation

$$\sum_\nu\left[\frac{1}{\xi}\hat{k}_\mu\hat{k}_\nu + D_{\mu\nu}(k)\right]G_{\nu\tau}(k) = \delta_{\mu\tau}. \tag{D13}$$

We simply do this numerically, inverting the four by four matrix for each k value.

To perform the perturbative expansion of the NDS action, we look at each term in turn. Consider

$$Q_{x,\rho;\xi} = \Omega^\dagger_{x,\rho;\xi}\Omega_{x,\rho;\xi}. \tag{D14}$$

Multiplying this out, we find that Q is a sum of loops of perimeter four and perimeter six, labeled P and E, respectively. The planar E loops, $E_{\mu\nu}$, are 1×2 loops extending in the $\pm\nu$ direction from site x. Hence,

$$Q = 1 + \alpha_3(1 - \alpha_3)\sum_j P_j + \frac{\alpha_3}{4}\sum_k E_k. \tag{D15}$$

Expanding each term out in terms of A's, we discover that $Q^{-1} = 1 - S_Q$ where now the expressions are quadratic functions of the gauge fields. Slightly abusing notation, we write P and E for the objects made of A_μ's, so that

$$S_Q = \alpha_3(1 - \alpha_3)\sum_j P_j + \frac{\alpha_3}{4}\sum_k E_k. \tag{D16}$$

Nearly identical results obtain for the other two Q's, with several small exceptions. First, the analogs of the plaquettes

TABLE XIV. Results of one loop lattice perturbation theory for selected observables, for the NDS action for several values of z. Uncertainties are ± 2 in the rightmost digit. Each one is interleaved with its momentum scale from Eq. (D27). The plaquette expectation is p. The quantities z_V, z_A, z_P and z_S are the renormalization factors for the local vector, axial vector, pseudoscalar, and scalar currents.

z	p	q^*	z_V	q^*	z_A	q^*	z_P	q^*	z_S	q^*
0	0.5	3.41	−1.38	1.68	−1.30	1.65	−0.12	2.28	0.04	2.31
0.008	0.504	3.41	−1.37	1.70	−1.30	1.66	−0.11	2.42	0.05	2.48
0.02	0.510	3.41	−1.38	1.71	−1.29	1.69	−0.12	2.48	0.04	2.54
0.05	0.525	3.41	−1.40	1.70	−1.31	1.69	−0.15	2.40	0.02	2.45
0.10	0.548	3.43	−1.42	1.74	−1.34	1.72	−0.19	2.70	−0.02	2.79

are built of one thin link $A_\mu(x)$ while the other three links are fattened. Second, the perimeter-six links are built entirely of fat links. Finally, in addition to the 1×2 $E_{\mu\nu}$ plaquettes, there are "chair" plaquettes $C_{\mu\nu\rho}$ which are "folded" about the μ axis. They extend in four directions $(\pm\nu, \pm\rho)$.

The analog of the fat to thin relation for the links $(U \to V)$ is a fat to thin gauge field relation,

$$B_\lambda(q) = \sum_\mu A_\lambda(q) h_{\mu\lambda}(q). \tag{D17}$$

This means that all the perimeter-six contributions can be easily computed beginning with the fat links, whose gauge-unfixed action is $D^0_{\mu\nu}(q)$. The thin link action is

$$D_{\mu\nu}(k) = \sum_{\lambda_1 \lambda_2} h_{\mu\lambda}(-q) D^0_{\lambda_1\lambda_2}(q) h_{\nu\lambda}(q). \tag{D18}$$

Finally, by convention the action $D_{\mu\nu}(q) \sim \delta_{\mu\nu}k^2 - k_\mu k_\nu$ so we have to rescale the action to remove explicit factors of the coupling constants, giving

$$S = \frac{1}{N}(P + z\tilde{Q}^{-1} + z\bar{Q}^{-1} + zQ^{-1}), \tag{D19}$$

where $N = 2N_c/(\beta g^2) = [1 + 2z(\alpha_1/3 + \alpha_2 + \alpha_3)]$, basically Eq. (D6).

The fattened terms in the action are awkward to compute. The plaquette is an example. It is probably best to record

$$F_{\mu\rho}(q) = i\hat{q}_\mu B_\rho(q) + A_\mu(q)\exp(-iq_\rho/2)$$
$$- B_\mu(q), \exp(iq_\rho/2) \tag{D20}$$

where B_μ is the fat link gauge potential, and then to substitute in Eq. (D17); to write (schematically)

$$F_{\mu\rho}(q) = \sum_\lambda A_\lambda(q) C_{\lambda\mu\nu}(q); \tag{D21}$$

and then

$$D_{\lambda_1\lambda_2}(q) = \sum_{\mu\nu} C_{\lambda_1\mu\nu}(-q) C_{\lambda_2\mu\nu}(q). \tag{D22}$$

We also need perturbative expressions for the partially fattened links. They are

$$\bar{A}_{\mu,\rho\eta}(q) = A_\mu(q) + \frac{\alpha_3}{2}[\hat{q}_\mu \hat{q}_\omega A_\omega(q) - \hat{q}^2_\omega A_\mu(q)], \tag{D23}$$

where $\omega \neq \mu, \nu, \rho$, and

$$\tilde{A}_{\mu,\rho}(q) = A_\mu(q) + \frac{\alpha_2}{2} \sum_{\eta \neq \mu,\rho} \hat{q}_\eta \left(1 + \alpha_3 - \hat{q}^2_\omega \frac{\alpha_3}{2}\right)$$
$$\times [A_\eta(q)\hat{q}_\mu - A_\mu(q)\hat{q}_\eta], \tag{D24}$$

where $\omega \neq \mu, \eta, \rho$.

Our simulations are done with $z = 1/125$. At that value of z, the perturbative properties of the NDS gauge action are almost indistinguishable from those of a pure Wilson action. Here are three examples.

First, the plaquette has an expansion $\mathrm{Tr}U_{\mathrm{plaq}}/N_c = 1 - g^2 p C_F$ where C_F is the quadratic Casimir for fundamentals and p is a constant. For the Wilson action, $p = 0.5$. This expression is often replaced by

$$-\ln\left\langle \frac{1}{N_c} \mathrm{Tr}U_{\mathrm{plaq}} \right\rangle = g^2 p C_F. \tag{D25}$$

This defines a coupling g^2 in the so-called α_V scheme, because the potential is written as

$$V(q) = -C_F \frac{4\pi \alpha_V(q)}{q^2}. \tag{D26}$$

The scale of the coupling is set by the Lepage-Mackenzie [54] prescription,

$$\log q^* = \frac{\int d^4q \log q I(q)}{\int d^4q I(q)}. \tag{D27}$$

Results for p and q^* for several values of z are given in Table XIV.

With the gluon propagator in hand we can immediately compute the static Coulomb potential. With our conventions, the continuum potential is $V(r) = 1/(4\pi r)$, and so plotting the rescaled lattice potential $4\pi r V(r)$ immediately exposes the lattice artifacts of a particular action. We show results for this quantity in Fig. 24 for $z = 1/125$, plotted together with the Wilson action result.
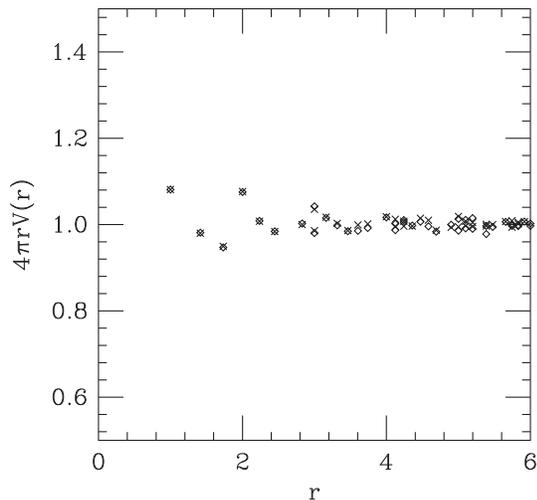
FIG. 24. Comparison of the potential for the NDS action, with $\gamma/\beta = 1/125$ (diamonds), with that of the usual Wilson action (crosses).

Last, we have the renormalization factors for currents. Calculations of matrix elements require a conversion to continuum regularization. We adopt the old tadpole-improved procedure of Lepage and Mackenzie [54]. In this scheme a continuum-regulated fermionic bilinear quantity $\bar{Q}$ with engineering dimension D [we have in mind finding the $\overline{\text{MS}}$ (modified minimal subtraction) value at scale μ] is related to the lattice value by

$$\bar{Q}(\mu = 1/a) = Q(a)\left(1 - \frac{3\kappa}{4\kappa_c}\right)Z_Q, \qquad \text{(D28)}$$

with

$$Z_Q = 1 + \alpha\frac{C_F}{4\pi}z_Q, \qquad \text{(D29)}$$

where $\alpha = g^2/(4\pi)$, C_F is the quadratic Casimir for the fermion, and z_Q is a scheme matching number. Results for nHYP clover fermions without the NDS term are tabulated in Ref. [55] and allow us to check the $z = 0$ limit. For more discussion of the calculation of the z_Q's, see Ref. [56]. Table XIV gives selected values of z_Q for the vector, axial vector, pseudoscalar, and scalar currents.

To evaluate the final Z-factors, we run $\alpha_V(q)$ obtained at $aq^\star = 3.43$ using the Lepage-Mackenzie prescription to the appropriate $aq^\star$ for each z_Q enumerated in the table. Running of α_V is carried out by numerical integration of the two-loop β-function,

$$\beta(\alpha_V) = q^2\frac{d\alpha_V}{dq^2} = -\beta_0\alpha_V^2 - \beta_1\alpha_V^3 - \cdots, \qquad \text{(D30)}$$

where the required coefficients for a theory with multiple fermion representations are [57]

$$\beta_0 = \frac{1}{3(4\pi)}\left(11C_2(G) - 2\sum_r N_r C_2(r)\right) \qquad \text{(D31)}$$

$$\beta_1 = \frac{1}{3(4\pi)^2}\left(34C_2(G)^2 - 2\sum_r N_r T(r)[5C_2(G) + 3C_2(r)]\right). \qquad \text{(D32)}$$

Here N_r denotes the number of Dirac flavors in representation r, while $T(r)$ and $C_2(r)$ are the standard trace and Casimir invariant for each representation. For our SU(4) multirep theory, we obtain $\beta_0 = 53/(24\pi)$ and $\beta_1 = 1531/(192\pi^2)$.

[1] J. B. Kogut, M. Stone, H. W. Wyld, J. Shigemitsu, S. H. Shenker, and D. K. Sinclair, Phys. Rev. Lett. **48**, 1140 (1982).

[2] J. B. Kogut, J. Shigemitsu, and D. K. Sinclair, Phys. Lett. B **145**, 239 (1984).

[3] F. Karsch and M. Lütgemeier, Nucl. Phys. **B550**, 449 (1999).

[4] H. Georgi and D. B. Kaplan, Phys. Lett. **145B**, 216 (1984).

[5] M. J. Dugan, H. Georgi, and D. B. Kaplan, Nucl. Phys. **B254**, 299 (1985).

[6] D. B. Kaplan, Nucl. Phys. **B365**, 259 (1991).

[7] G. Ferretti, J. High Energy Phys. 06 (2014) 142.

[8] G. Ferretti and D. Karateev, J. High Energy Phys. 03 (2014) 077.

[9] T. DeGrand and Y. Liu, Phys. Rev. D **94**, 034506 (2016); **95**, 019902(E) (2017).

[10] T. DeGrand, Y. Liu, E. T. Neil, Y. Shamir, and B. Svetitsky, Phys. Rev. D **91**, 114502 (2015).

[11] T. A. DeGrand, D. Hackett, W. I. Jay, E. T. Neil, Y. Shamir, and B. Svetitsky, *Proc. Sci.*, LATTICE2016 (2016) 219.

[12] T. DeGrand, M. Golterman, E. T. Neil, and Y. Shamir, Phys. Rev. D **94**, 025020 (2016).

[13] G. Ferretti, J. High Energy Phys. 06 (2016) 107.

[14] A. Belyaev, G. Cacciapaglia, H. Cai, G. Ferretti, T. Flacke, A. Parolini, and H. Serodio, J. High Energy Phys. 01 (2017) 094; 12 (2017) 088.

[15] M. E. Peskin, Nucl. Phys. **B175**, 197 (1980).

[16] A. Hasenfratz and F. Knechtli, Phys. Rev. D **64**, 034504 (2001).

[17] A. Hasenfratz, R. Hoffmann, and S. Schaefer, J. High Energy Phys. 05 (2007) 029.

[18] C. W. Bernard and T. A. DeGrand, Nucl. Phys. B, Proc. Suppl. **83–84**, 845 (2000).

[19] Y. Shamir, B. Svetitsky, and E. Yurkovsky, Phys. Rev. D **83**, 097502 (2011).

[20] T. DeGrand, Y. Shamir, and B. Svetitsky, Phys. Rev. D **90**, 054501 (2014).

[21] V. Ayyar, T. DeGrand, D. C. Hackett, W. I. Jay, E. T. Neil, Y. Shamir, and B. Svetitsky, arXiv:1802.09644.

[22] A. Hasenfratz, Y. Liu, and C. Y.-H. Huang, arXiv:1507.08260.

[23] M. Lüscher, J. High Energy Phys. 08 (2010) 071; 03 (2014) 092.

[24] A. Bazavov *et al.* (MILC Collaboration), Phys. Rev. D **93**, 094510 (2016).

[25] T. DeGrand, Phys. Rev. D **95**, 114512 (2017).

[26] M. Cè, M. G. Vera, L. Giusti, and S. Schaefer, Phys. Lett. B **762**, 232 (2016).

[27] S. R. Sharpe and R. L. Singleton, Jr., Phys. Rev. D **58**, 074501 (1998).

[28] O. Bär, G. Rupak, and N. Shoresh, Phys. Rev. D **70**, 034508 (2004).

[29] G. Rupak and N. Shoresh, Phys. Rev. D **66**, 054503 (2002).

[30] S. Aoki, Phys. Rev. D **68**, 054508 (2003).

[31] S. Sharpe, arXiv:hep-lat/0607016.

[32] M. Golterman, arXiv:0912.4042.

[33] O. Bär and M. Golterman, Phys. Rev. D **89**, 034505 (2014); **89**, 099905 (2014).

[34] J. Bijnens and J. Lu, J. High Energy Phys. 11 (2009) 116.

[35] S. Aoki, O. Bär, and S. R. Sharpe, Phys. Rev. D **80**, 014506 (2009).

[36] A. Bazavov *et al.* (MILC Collaboration), Rev. Mod. Phys. **82**, 1349 (2010).

[37] M. Bruno, T. Korzec, and S. Schaefer, Phys. Rev. D **95**, 074504 (2017).

[38] M. E. Peskin and T. Takeuchi, Phys. Rev. D **46**, 381 (1992).

[39] K. Kawarabayashi and M. Suzuki, Phys. Rev. Lett. **16**, 255 (1966).

[40] Riazuddin and Fayyazuddin, Phys. Rev. **147**, 1071 (1966).

[41] R. C. Johnson, Nucl. Phys. **B23**, 247 (1970).

[42] T. A. DeGrand, M. Golterman, W. I. Jay, E. T. Neil, Y. Shamir, and B. Svetitsky, Phys. Rev. D **94**, 054501 (2016).

[43] M. Golterman and Y. Shamir, Phys. Rev. D **91**, 094506 (2015).

[44] M. Golterman and Y. Shamir, arXiv:1707.06033.

[45] T. DeGrand and S. Schaefer, arXiv:0712.2914.

[46] P. Lepage and C. Gohlke, gplepage/lsqfit: lsqfit version 9.1.3, 2017.

[47] P. Lepage and D. Hackett, gplepage/gvar: gvar version 8.3.2, 2017.

[48] K. M. Bitar *et al.*, Phys. Rev. D **42**, 3794 (1990).

[49] R. Brower, S. Chandrasekharan, J. W. Negele, and U. J. Wiese, Phys. Lett. B **560**, 64 (2003).

[50] S. Aoki, H. Fukaya, S. Hashimoto, and T. Onogi, Phys. Rev. D **76**, 054508 (2007).

[51] J. Gasser and H. Leutwyler, Phys. Lett. B **184**, 83 (1987).

[52] S. R. Sharpe and J. M. S. Wu, Phys. Rev. D **71**, 074501 (2005).

[53] P. Weisz, Nucl. Phys. **B212**, 1 (1983).

[54] G. P. Lepage and P. B. Mackenzie, Phys. Rev. D **48**, 2250 (1993).

[55] T. A. DeGrand, A. Hasenfratz, and T. G. Kovacs, Phys. Rev. D **67**, 054501 (2003).

[56] T. A. DeGrand, Phys. Rev. D **67**, 014507 (2003).

[57] Y.-L. Shi and R. Shrock, Phys. Rev. D **92**, 125009 (2015).